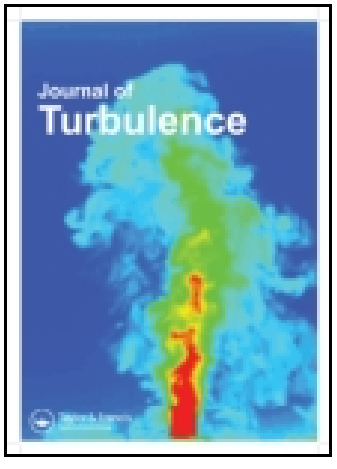

Journal of Turbulence
Publication details, including instructions for authors and subscription information:
http://www.tandfonline.com/loi/tjot20

RANS and LES computations of the tip-leakage vortex for different gap widths

J. Decaix[a], G. Balarac[b], M. Dreyer[c], M. Farhat[c] & C. Münch[a]

[a] Design and Materials Unit, University of Applied Sciences Western Switzerland, Sion, Switzerland

[b] LEGI, Univ. Grenoble Alpes, CNRS, Grenoble, France

[c] Laboratory for Hydraulic Machines, Ecole Polytechnique Fédérale de Lausanne, Lausanne, Switzerland

Published online: 23 Jan 2015.

Journal of Turbulence, 2015
Vol. 16, No. 4, 309–341, http://dx.doi.org/10.1080/14685248.2014.984068

RANS and LES computations of the tip-leakage vortex for different gap widths

J. Decaix[a*], G. Balarac[b], M. Dreyer[c], M. Farhat[c] and C. Münch[a]

[a]*Design and Materials Unit, University of Applied Sciences Western Switzerland, Sion, Switzerland;* [b]*LEGI, Univ. Grenoble Alpes, CNRS, Grenoble, France;* [c]*Laboratory for Hydraulic Machines, Ecole Polytechnique Fédérale de Lausanne, Lausanne, Switzerland*

(*Received 22 July 2014; accepted 30 October 2014*)

In hydraulic turbines, the tip-leakage vortex is responsible for flow instabilities and for promoting erosion due to cavitation. To better understand the tip vortex flow, Reynolds-averaged Navier–Stokes (RANS) and large eddy simulation (LES) computations are carried out to simulate the flow around a NACA0009 blade including the gap between the tip and the wall. The main focus of the study is to understand the influence of the gap width on the development of the tip vortex, as for instance its trajectory. The RANS computations are performed using the open source solver OpenFOAM 2.1.0, two incidences and five gaps are considered. The LESs are achieved using the YALES2 solver for one incidence and two gaps.

The validation of the results is performed by comparisons with experimental data available downstream the trailing edge. The position of the vortex core, the mean velocity and the mean axial vorticity fields are compared at three different downstream locations. The results show that the mean behaviour of the tip vortex is well captured by the RANS and LES computations compared to the experiment. The LES results are also analysed to bring out the influence of the gap width on the development of the tip-leakage vortex. Finally, a law that matches the vortex trajectory from the leading edge to the mid-chord is proposed. Such a law can be helpful to determine, in case of cavitation, if the tip vortex will interact with the walls and cause erosion.

Keywords: tip-leakage vortex; dynamic Smagorinsky model; $k - \omega$ SST; YALES2; OpenFOAM; vortex trajectory

1. Introduction

The tip-leakage vortex occurs in the gap between the blade tip and the endwall. It can be encountered in aircraft engines,[1] axial pumps [2] or hydraulic turbines.[3]

First studies, devoted to the tip clearance flow, focus on the head losses and the ability of the tip vortex to promote cavitation in hydraulic pumps.[4] In the 1980s, Lakshminarayana and co-workers carried out experiments on an axial compressor rotor.[5–11] These studies allow to depict the main features of the tip clearance flow. The leakage flow occurs on the suction side between 25% and 50% of the chord length and involves a low-momentum region.[6,9] In the low-momentum region, the turbulence level [7] is high and increases with distance downstream. Furthermore, it is revealed that the radial turbulence intensities dominate compared to the two other components. However, these experiments do not show the low-momentum region as an organised tip-leakage vortex except for a ratio

*Corresponding author. Email: jean.decaix@hevs.ch

between the gap τ and the chord length c larger than $\tau/c = 0.034$. This observation is in opposition with those performed by other authors,[12–16] who put in evidence a tip-leakage vortex. For instance, in a series of papers, Kang et al. [14,15,17] described the tip clearance flow in a blade cascade. They observed the tip-leakage vortex as also a tip-separation vortex that occurs at the pressure side and then moves to the suction side. Moreover, a secondary vortex located between the tip blade suction side and the tip-leakage vortex is mentioned. This vortex has a counter-rotative motion compared to the tip-leakage vortex.

More recently, several experiments were carried out at Virginia Tech downstream a compressor blade cascade.[1,18] Several gap widths are investigated with and without an endwall motion. The endwall motion does not modify strongly the main features of the flow. Without the endwall motion and just downstream the trailing edge, the core of the vortex presents a deficit in axial velocity of approximately 45%. Moreover, an induced vortex with an axial vorticity with an opposite sign to the tip-leakage vortex is located between the tip vortex and the endwall. Regarding the turbulent flow, the turbulent field is anisotropic since the streamwise and the pitchwise turbulent stresses dominate the spanwise turbulent stresses by an amount of approximately 20%. It is also put in evidence that the maximum of turbulent kinetic energy and production of kinetic energy is located on an arc surrounding the vortex. The cross gradient of the mean axial velocity is the main contributor to the production of turbulent kinetic energy. Such features are also observed further downstream. A change in the gap width does not modify the flow topology even if the position of the vortex differs. The increase in gap width leads to an increase in the vortex size and strength (about a factor of 4 between the two extreme gaps). Nevertheless, the deficit in axial velocity is not changed, whereas the magnitude of the mean velocity gradient and therefore the production of turbulent kinetic energy decreases.

Numerical investigations are only performed for two decades. Several attempts have been performed with Reynolds-averaged Navier–Stokes (RANS) computations using standard eddy viscosity models.[19–21] Such models as the $k - \omega$ shear-stress transport (SST) are able to capture the global features of a compressor cascade as for instance the tip vortex size and trajectory.[21] Furthermore, the mean cross-flow distribution is also predicted accurately.[20] Nevertheless, due to their assumptions, these models fail to predict accurately the turbulence field in the tip clearance area. For this reason, enhanced RANS models as non-linear eddy viscosity models [22] or second-moment closure [23] have been used. These models improve the flow prediction in the blade passage through an accurate capture of the swirling flow compared to the eddy viscosity models. Furthermore, the turbulence field provided is different. For instance, the non-linear eddy viscosity model reduced the peak of turbulence captured by the eddy viscosity models due to the combined stress tensor sensitivity to strain and vorticity. However, some difficulties are still encountered close to the wall by all the RANS computations due to the use of wall laws or damping functions. To avoid assumptions at the wall, large eddy simulations (LESs) have also been attempted. The ones carried out by You et al. [24–27] are well documented and focus on the experimental cases studied by Muthanna and Wang.[1,18] Comparisons with the experiment are performed only through the position of the vortex core downstream the blade cascade. Nevertheless, the extensive study of the flow in the tip gap clearance area matches the conclusions drawn by the experiment. For instance, the turbulent stresses are anisotropic with a dominance of the streamwise and pitchwise components. The main contribution to the production of turbulent kinetic energy arises from the cross gradient of the mean axial velocity. Contrary to the experimental measurements, the LES computations show that a decrease in the tip gap width involves a diminution of the axial velocity deficit.

The major part of the above-mentioned studies concerns air compressor flows. Regarding the hydraulic flows, and more precisely hydraulic turbines, the tip-leakage vortex is known to promote flow instabilities, cavitation and erosion due to the collapse of the cavitation bubbles close to the walls. The behaviour of the tip-leakage vortex, as for instance its trajectory,[3] is not well understood. Therefore, to answer these questions, a NACA0009 profile mounted in a water channel flow is investigated using RANS and LES computations. Reynolds stress models with low Reynolds and wall effects are not considered in this paper. Indeed, in this study, the RANS simulations are used to capture the mean global features of the vortex flow (for instance, the vortex position), whereas the LESs are dedicated to study the vortex formation in the gap region. Since the incidence of the blade and the flow curvature are relatively low, second-moment closure models are not expected to strongly improve the results compared to the RANS simulations, at least regarding the mean flow behaviour.

The first two parts of the paper describe the numerical tools and the test case. Then, the result analysis is divided into three subsections: the first one is devoted to the assessment of the simulations compared to the experimental measurements,[28] the second sub-part focuses on the influence of the gap width on the flow structure and the last one focuses on the development of a law that matches the tip vortex trajectory over the first steps of its development whatever is the gap width.

2. Governing equations and numerical tools

The incompressible turbulent flow considered in this study is governed by the instantaneous Navier–Stokes equations expressing mass and momentum conservation,

$$\begin{cases} \dfrac{\partial u_i}{\partial x_i} = 0, \\ \dfrac{\partial u_i}{\partial t} + \dfrac{\partial u_i u_j}{\partial x_j} = -\dfrac{1}{\rho}\dfrac{\partial p}{\partial x_i} + \dfrac{\partial}{\partial x_j}\left(\nu \dfrac{\partial u_i}{\partial x_j}\right), \end{cases} \tag{1}$$

where u_i, p, ρ and ν are respectively the velocity components, the pressure, the (constant) density and kinematic viscosity. The RANS approach solves only the mean flow and attempts to model the fluctuating field. The governing equations take the following form:

$$\begin{cases} \dfrac{\partial \langle u_i \rangle}{\partial x_i} = 0, \\ \dfrac{\partial \langle u_i \rangle \langle u_j \rangle}{\partial x_j} = -\dfrac{1}{\rho}\dfrac{\partial \langle p \rangle}{\partial x_i} + \dfrac{\partial}{\partial x_j}\left((\nu + \nu_T)\dfrac{\partial \langle u_i \rangle}{\partial x_j}\right), \end{cases} \tag{2}$$

where $\langle u_i \rangle$ denotes the time-averaged velocity field components and $\langle p \rangle$ is the mean pressure. The influence of the fluctuations on the mean flow is taken into account by a turbulent viscosity assumption, ν_T. In this work, the turbulent viscosity is calculated with the $k - \omega$ SST model proposed by Menter.[29] Moreover, the walls are taken into account through an extended wall law approach:

$$u^+ = y^+ \quad \text{if} \quad y^+ < 11 \tag{3}$$

$$u^+ = \frac{1}{\kappa} \ln y^+ + 5.25 \quad \text{if} \quad y^+ > 11 \tag{4}$$

RANS computations are performed using the OpenFOAM 2.1.0 solver,[30] which is an open source solver. For the present study, the stationary incompressible RANS equations are solved using the pressure/velocity coupling algorithm SIMPLE (Semi-Implicit Method for Pressure Linked Equations) proposed by Patankar.[31]To avoid spatial oscillations of the pressure field over the collocated grid arrangement, Rhie and Chow pressure-weighted interpolation is applied.[32] The convective terms are discretised using the 'limitedLinear' scheme, which is a total variation diminishing scheme [33] specific to the OpenFOAM solver.

LES approach solves only the filtered velocity field $\bar{u}_i$, where the filtering operation allows to separate the scales of the flow motion at the grid level, with the small motion scales taken into account by a subgrid-scale model. The filtered velocity field is computed as the solution of the filtered Navier–Stokes equations:

$$\begin{cases} \dfrac{\partial \bar{u}_i}{\partial x_i} = 0, \\ \dfrac{\partial \bar{u}_i}{\partial t} + \dfrac{\partial \bar{u}_i\, \bar{u}_j}{\partial x_j} = -\dfrac{1}{\rho}\dfrac{\partial \bar{p}}{\partial x_i} + \dfrac{\partial}{\partial x_j}\left((\nu + \nu_{\mathrm{SGS}})\dfrac{\partial \bar{u}_i}{\partial x_j}\right), \end{cases} \tag{5}$$

where the eddy viscosity ν_{SGS} must be defined to close the system (5). The localised dynamic Smagorinsky model [34] is used in this study. The eddy viscosity is computed as $\nu_{\mathrm{SGS}} = (C\ \Delta)^2\ \left|\bar{S}(x,t)\right|$, where $\left|\bar{S}(x,t)\right|$ is the norm of the filtered strain rate tensor. The C coefficient is dynamically computed following Germano's definition.[34] In this work, LES computations are carried out with the YALES2 incompressible fractional-step solver.[35,36] The boundary condition at the wall is based on a non-equilibrium wall law.[37,38] Compared to the wall law used for the RANS computations, such a law takes into account the pressure gradient, which is a key term to correctly compute non-equilibrium boundary layers.[39] Furthermore, this approach does not assume that the boundary layer is turbulent contrary to the RANS modelling.

3. Test case

The hydrofoil is made of a NACA0009 with an original chord of $c_0 = 0.11$ m and a span of 0.15 m.[40] The shape of the blade is computed using Equation (7).

$$\frac{y_b}{c_0} = a_0\left(\frac{x}{c_0}\right)^{1/2} + a_1\left(\frac{x}{c_0}\right) + a_2\left(\frac{x}{c_0}\right)^2 + a_3\left(\frac{x}{c_0}\right)^3 \quad \text{for} \quad 0 \le \frac{x}{c_0} \le 0.5 \tag{6}$$

$$\frac{y_b}{c_0} = b_0 + b_1\left(1 - \frac{x}{c_0}\right) + b_2\left(1 - \frac{x}{c_0}\right)^2 + b_3\left(1 - \frac{x}{c_0}\right)^3 \quad \text{for} \quad 0.5 \le \frac{x}{c_0} \le 1 \tag{7}$$

with

$$\begin{array}{llllllll} a_0 = 0.1737 & a_1 & = -0.2422 & a_2 & = 0.3046 & a_3 & = -0.2657 \\ b_0 = 0.0004 & b_1 & = 0.1737 & b_2 & = -0.1898 & b_3 & = 0.0387 \end{array}$$

In the present case, the blade is truncated, therefore the chord is reduced to $c = 0.1$ m. This hydrofoil is mounted in the channel of the EPFL high-speed cavitation tunnel, which is a close loop with a test section measuring $0.15 \times 0.15 \times 0.750$ m^3.[41] The incidence of

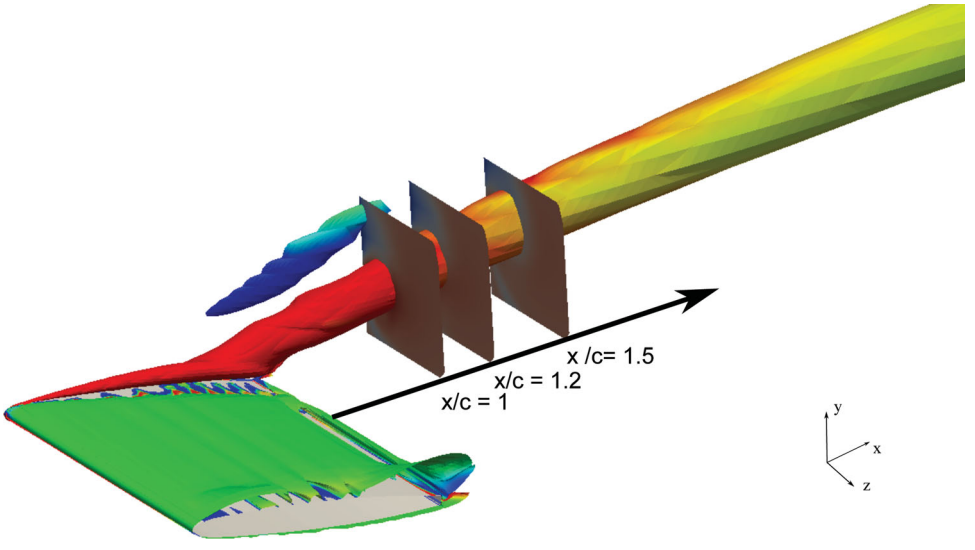

Figure 1. Tip vortex visualisation using the Q-criterion.

the profile can be set to different values and the gap τ between the blade tip and the wall can evolve between $\tau/c = 0$ and $\tau/c = 0.2$. The Reynolds number based on the blade chord is $\mathrm{Re}_c = 10^6$, with an inlet normal uniform velocity $u_{\mathrm{inlet}} = 10.2$ m/s. The experimental data are available at three downstream locations $x/c = 1$, $x/c = 1.2$ and $x/c = 1.5$ (Figure 1). The velocity measurements are performed using stereo particle image velocimetry. The set-up is based on a YAG laser providing a 2 mm wide laser sheet perpendicular to the vortex axis. Pairs of images are acquired using two cameras viewing the scene with a 30° angular shift.

Several computations have been performed (Table 1) for different incidences and gap widths.

For the RANS computations, the computational domain (Figure 2) extends 5 chords upstream the leading edge and 10 chords downstream the trailing edge. A structured mesh with approximately 2.8 million nodes is used. The gap width is discretised with 15 points for the gaps $\tau/c = 0.02$ and $\tau/c = 0.03$ and 30 points for the other gaps. The inlet normal velocity is fixed uniform and is taken equal to $u_{\mathrm{inlet}} = 10.2$ m/s. This value is used as reference for the non-dimensional values of the velocity field and other quantities such as the vorticity field or the Q-criterion. A uniform outlet pressure is specified to $p_{\mathrm{outlet}} = 0$. The turbulent intensity is set to 5%.

To decrease the computation time, LESs are carried out on a reduced domain (Figure 2) that extends two chords upstream the leading edge and five chords downstream the trailing edge. For these simulations, a non-structured mesh is used with 200 million elements for the

Table 1. Flow configurations computed with RANS (Δ) and LES (◇).

Incidence i \ Gap τ/c	0.02	0.03	0.05	0.1	0.15
5°	Δ	Δ	Δ	Δ	Δ
10°	Δ ◇	Δ	Δ	Δ ◇	Δ

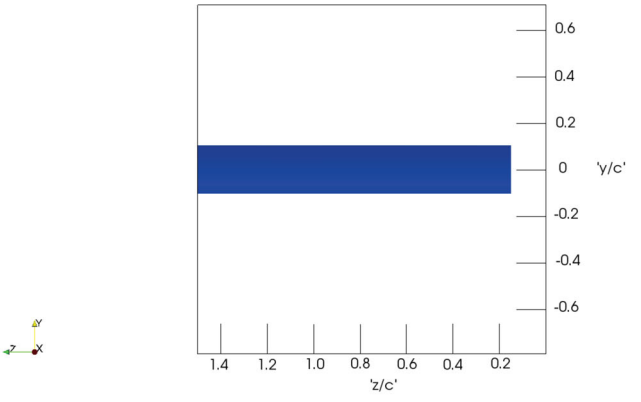

Downstream view, idem for RANS and LES.

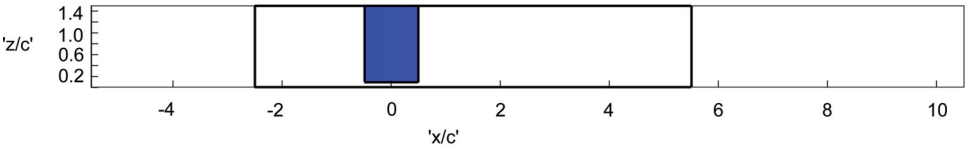

Top view, RANS domain (thin line) and LES domain (thick line).

Figure 2. Computational domains.

gap $\tau/c = 0.1$ and 300 million elements for the gap $\tau/c = 0.02$. The inlet velocity condition is specified by interpolating the velocity profile extracted from the RANS computations. At the outlet, a mean pressure profile is set. As the turbulence level in the channel is low, no fluctuating part is added to the mean inlet profile. The boundary layers are not enough refined to ensure a y^+ of 1, therefore the wall law is used.[37,38]

For both RANS and LES computations, the y^+ values on the NACA profile are around 20 in average with maximal values close to 60.

4. Results

4.1. *Validation of the computations*

Validation of RANS and LES computations iscarried out for one incidence (10°) and two gaps ($\tau/c = 0.02$ and $\tau/c = 0.1$) by comparisons with experimental data.

The contours of each velocity component at the first experimental plane (i.e. $x/c = 1$) are displayed in Figures 3–5 for the gap $\tau/c = 0.02$ and in Figures 6–8 for the gap $\tau/c = 0.1$.

For the gap $\tau/c = 0.02$, the deficit of the axial velocity u_x^* in the core of the vortex is well predicted by the numerical simulations compared to the experimental results (Figure 3). Nevertheless the vortex core is larger in the computations than in the experiment and the magnitude of the velocity at the vortex centre is slightly higher for the computations than the experiment. For the transversal components u_y^* and u_z^*, the global features are well predicted (Figures 4 and 5). For the pitchwise component, the positive magnitude close to the wall is in agreement with the experiment whereas the negative magnitude is slightly

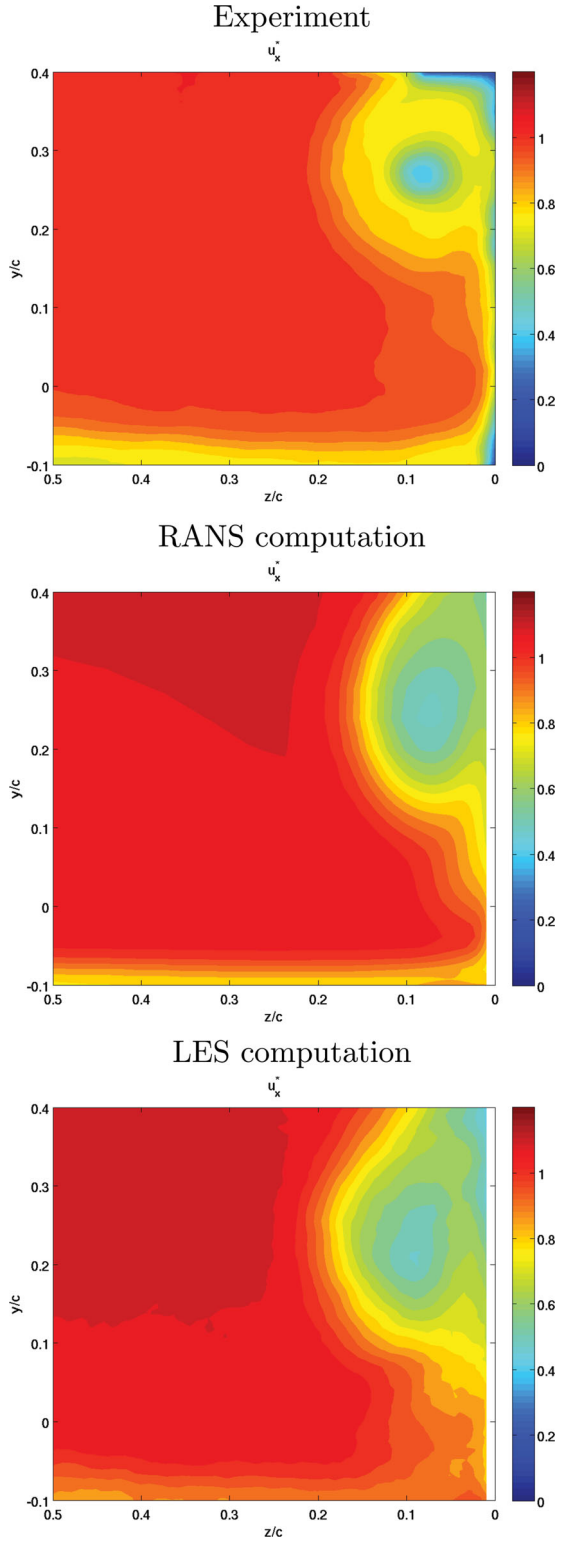

Figure 3. Contours of the non-dimensional axial velocity component at $x/c = 1$ and for the gap $\tau/c = 0.02$.

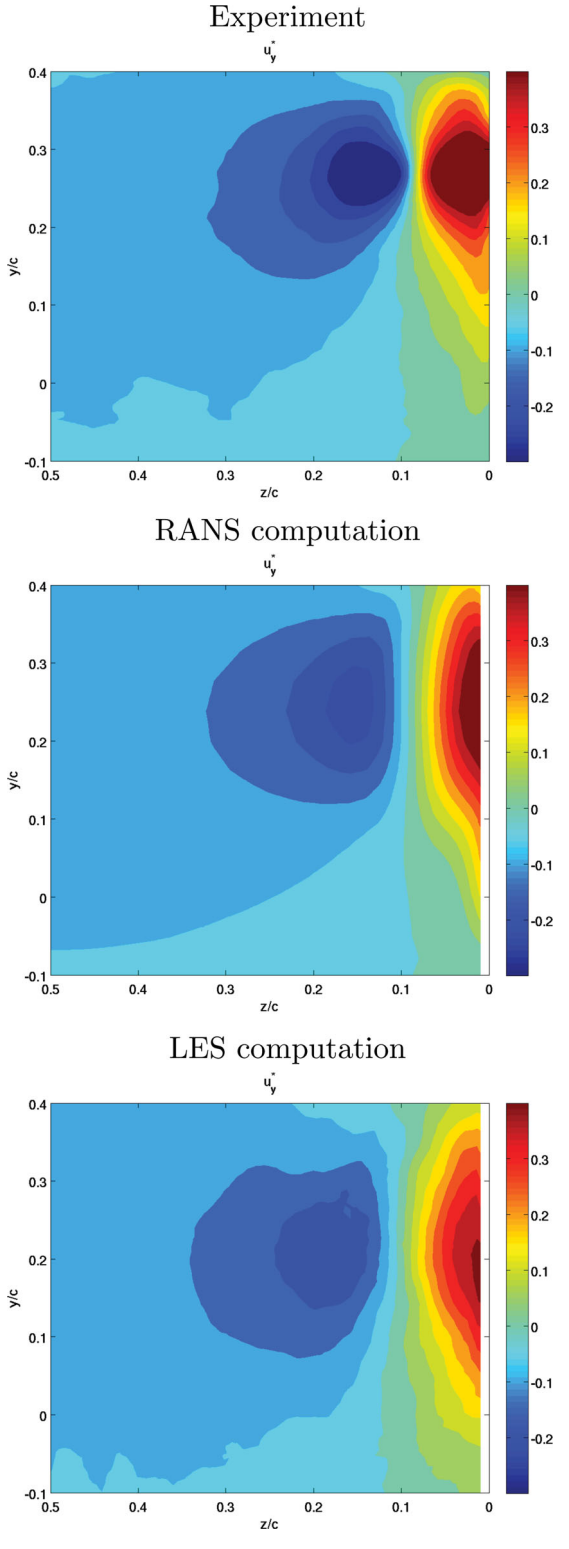

Figure 4. Contours of the non-dimensional pitchwise velocity component at $x/c = 1$ and for the gap $\tau/c = 0.02$.

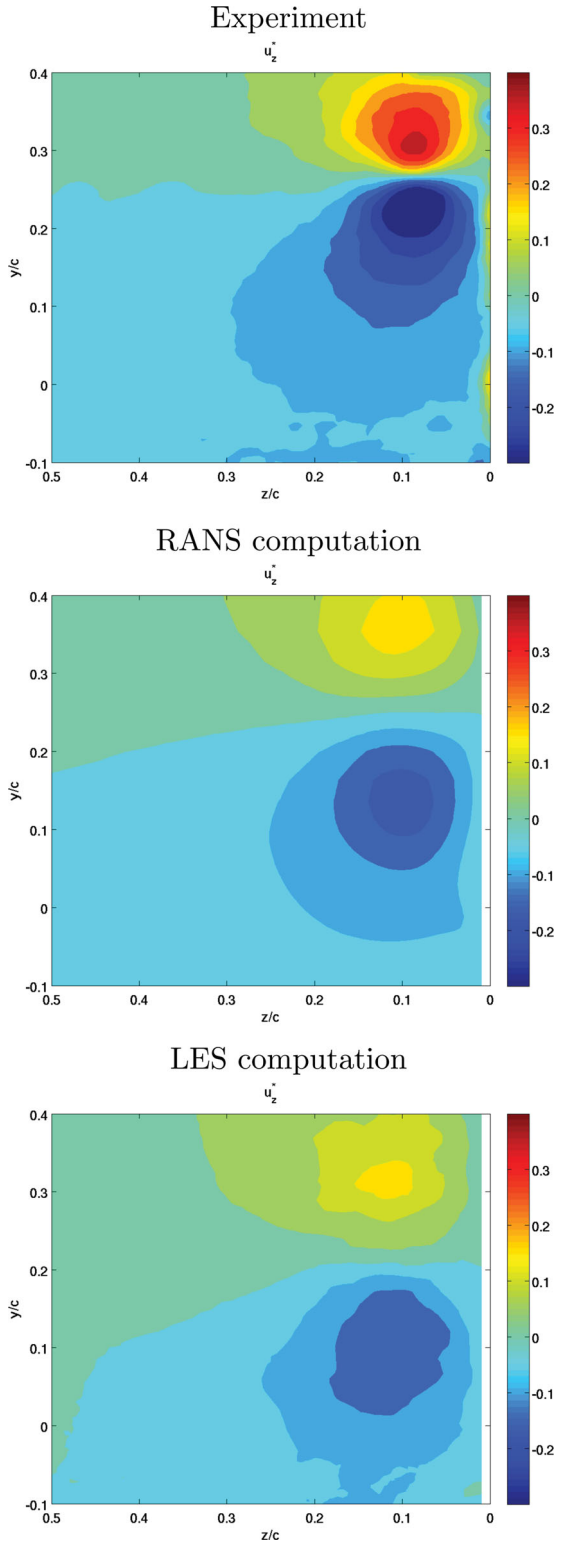

Figure 5. Contours of the non-dimensional spanwise velocity component at $x/c = 1$ and for the gap $\tau/c = 0.02$.

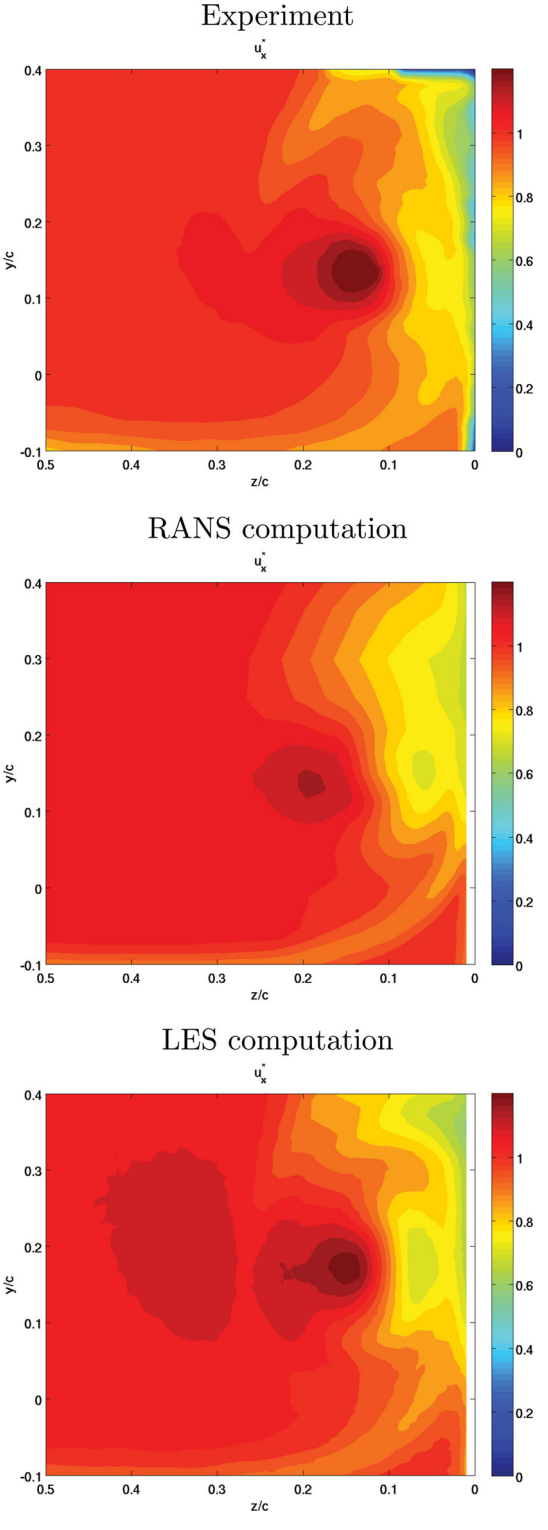

Figure 6. Contours of the non-dimensional axial velocity component at $x/c = 1$ and for the gap $\tau/c = 0.1$.

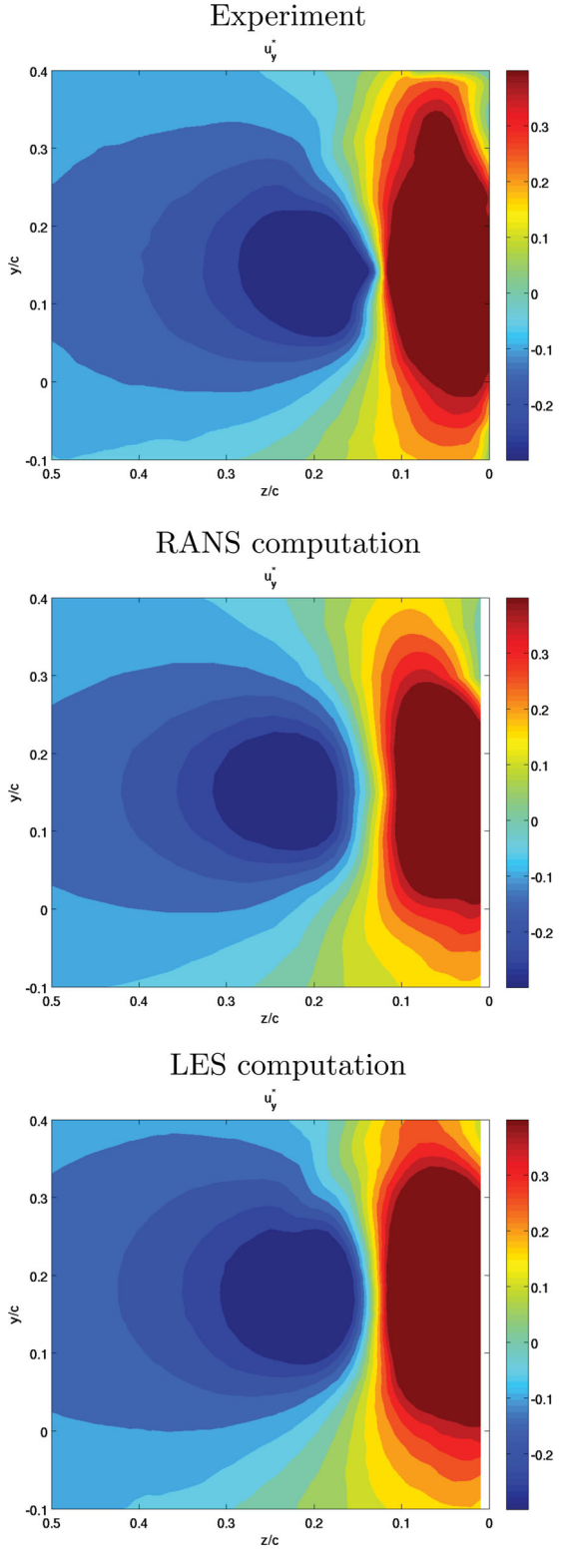

Figure 7. Contours of the non-dimensional pitchwise velocity component at $x/c = 1$ and for the gap $\tau/c = 0.1$.

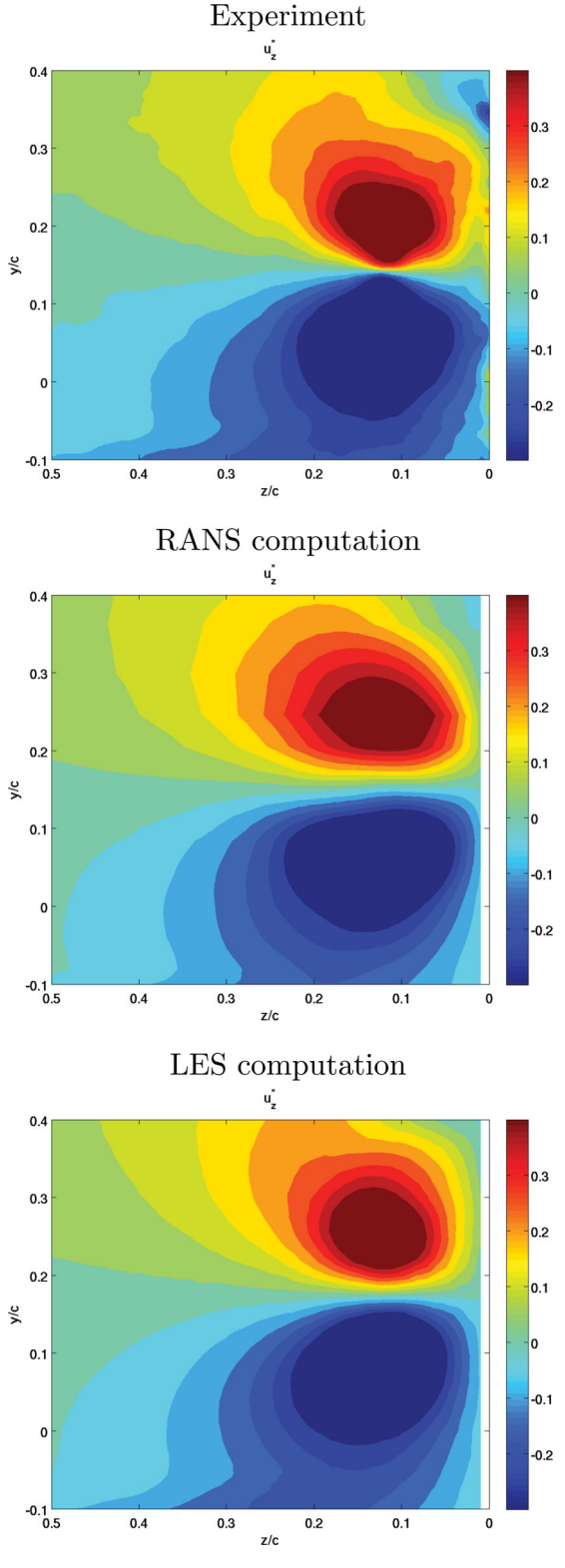

Figure 8. Contours of the non-dimensional spanwise velocity component at $x/c = 1$ and for the gap $\tau/c = 0.1$.

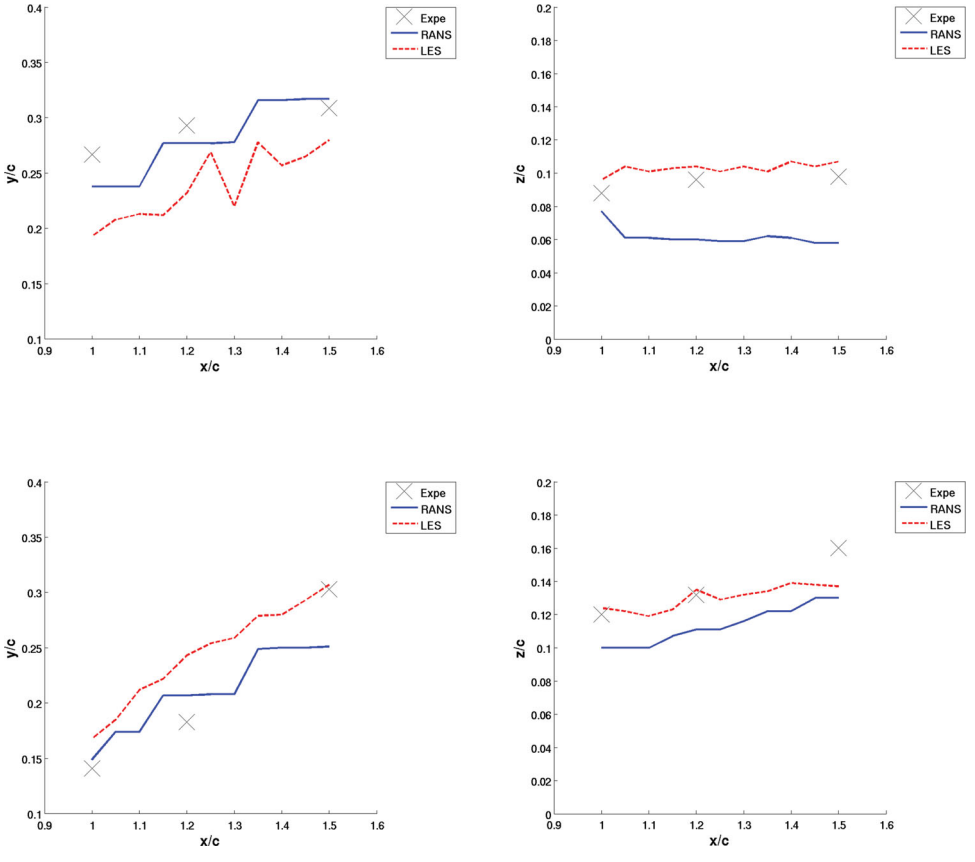

Figure 9. Position of the vortex centre. $\tau/c = 0.02$ (top) and $\tau/c = 0.1$ (bottom).

underestimated by the computations. The spanwise component is further diffused by the computations, which can be the result of a too coarse mesh in the spanwise direction.

For the gap $\tau/c = 0.1$, the axial velocity does not show a deficit in the core of the vortex as for the case $\tau/c = 0.02$ (Figure 6). On the contrary, an excess of the axial velocity is present in the region of the vortex centre but not exactly at the vortex centre. For the transversal components, the computations provide the same topology and velocity magnitude as the experiment. However, the computations show a vortex core slightly larger than in the experiment since the spanwise (respectively pitchwise) gradient of the pitchwise (respectively spanwise) velocity component around the vortex centre spreads on a larger band. This is more visible for the RANS computation than for the LES one.

The position of the vortex centre determined using the maximum of the axial vorticity is plotted in Figure 9 for the two gaps. The position is projected on an x–y plane (pitchwise position) and on an x–z plane (spanwise position). More precisely, the position of the vortex corresponds to the coordinates y and z of the cell centre at a specific x position. Therefore, as long as the vortex is located in the same cell, the y and z coordinates do not change, which explains the step by step evolution of the vortex position in the case of the RANS computations. Furthermore, as the cells are not aligned with the vortex trajectory, sudden variations can arise as for instance in the case of the LES computation for the gap $\tau/c = 0.02$. Beyond these remarks, for the gap $\tau/c = 0.02$, the LES computation underestimates

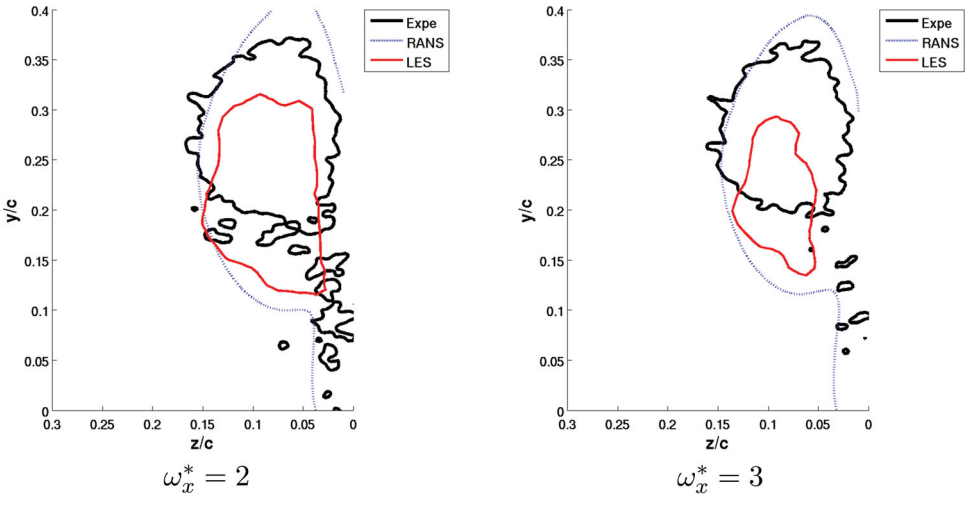

Figure 10. Iso-lines of the non-dimensional axial vorticity ω_x^* for the gap $\tau/c = 0.02$ at $x/c = 1$.

the pitchwise position of the vortex centre compared with the RANS computation and the experiment. The spanwise position is well predicted by the LES computation compared with the experiment. The RANS computation shows a vortex that evolves closer to the wall than the experiment. For the second gap $\tau/c = 0.1$, the computations provide a pitchwise position in accordance with the experiment. The spanwise position is once again closer to the wall for the RANS computation.

The vorticity field is then analysed by plotting two iso-values of the axial vorticity $\omega_x^* = (\omega_x c)/u_{\text{inlet}}$ close to the vortex centre (Figures 10 and 11). For the gap $\tau/c = 0.02$, the vorticity field is perturbed by the presence of the wall. The iso-line does not defined a circle around the vortex centre but embraces also the boundary layer. The iso-line $\omega_x^* = 2$

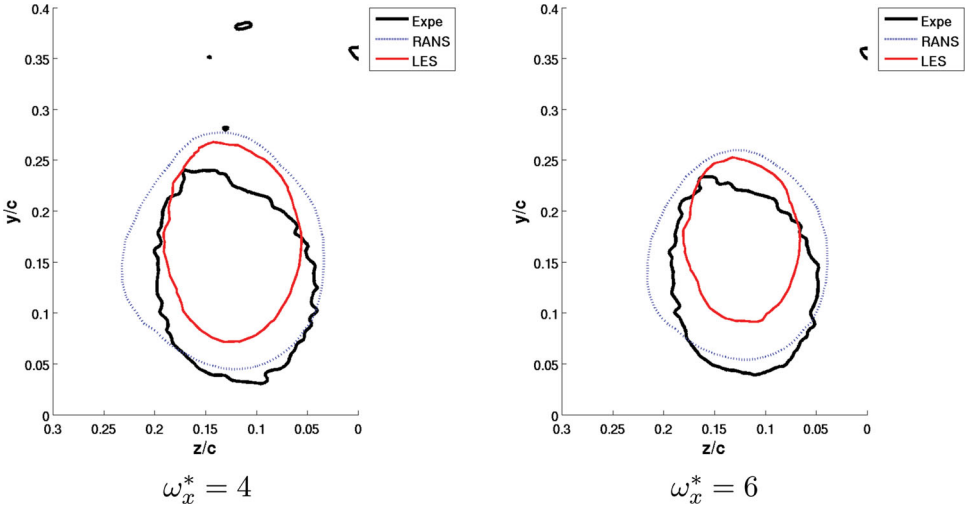

Figure 11. Iso-lines of the non-dimensional axial vorticity ω_x^* for the gap $\tau/c = 0.1$ at $x/c = 1$.

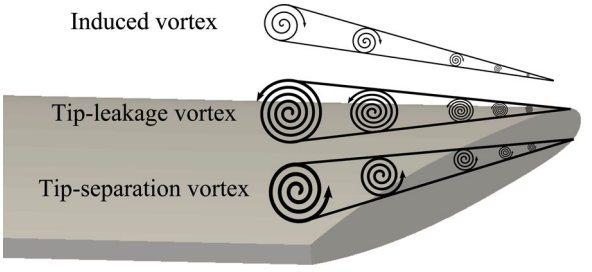

Figure 12. Schematic view of the flow structure in the gap region from [27].

provided by the RANS computation covers the same region as the experimental one. For the LES computation, only the vortex is delimited by the iso-line, whereas the boundary layer does not present a high level of vorticity. Increasing the value to $\omega_x^* = 3$, the LES computation shows a smaller region of high vorticity than the experiment and the RANS computation. The use of the wall law for the LES computation may explain the lower magnitude of the axial vorticity. For the gap $\tau/c = 0.1$, the region of high vorticity is nearly the same for the computations and the experiment.

To conclude, the computations are able to provide mean quantities in accordance with the experimental measurements. Therefore, the computations can be used with confidence to explore the flow in the gap region where experimental data are not available.

4.2. *Flow topology in the gap*

The flow topology in the gap is analysed using the LES data for the incidence of 10° and for two gaps $\tau/c = 0.02$ and $\tau/c = 0.1$.

The pressure difference between the pressure side and the suction side induces a secondary jet flow at the tip blade. Due to the freestream flow and the spanwise equalisation of the pressure gradient on the pressure side, the secondary jet flow can not evolve indefinitely along the spanwise direction and therefore rolls up to form the tip vortex. The resulting vortex structure evolves downstream influenced by the endwall and the blade. In the LES of a compressor cascade carried out by You et al. [26,27] a denomination of the vortices is proposed with the presence of respectively a tip-leakage vortex, an induced vortex and one or further tip-separation vortices (Figure 12). The tip-leakage vortex is formed due to the rolling up of the tip-leakage jet [42] and interacts with the endwall. The induced vortex results from the interaction between the tip-leakage vortex and the wall boundary layer leading to the roll-up of a part of the boundary layer in a counter-rotative motion compared with the tip-leakage vortex. The tip-separation vortices are formed due to separation of the flow at the pressure side of the blade. Experimentally, the tip-separation vortices are not well documented due to the lack of resolution of the experimental apparatus. However, the tip-leakage vortex concentrates the larger amount of axial vorticity compared with the two other vortices and seems to dominate the flow structure.

For the present flow configuration, the flow structure depends on the gap width. It is noticeable that the two gap widths computed are close to the extrema configurations computed by You et al.,[26] which correspond to $\tau/c \approx 0.02$ and $\tau/c \approx 0.08$ using the same reference scales.

Figures 13 and 14 display instantaneous and mean vortex structures for each gap using an iso-surface of the Q-criterion coloured by the axial vorticity. The instantaneous views

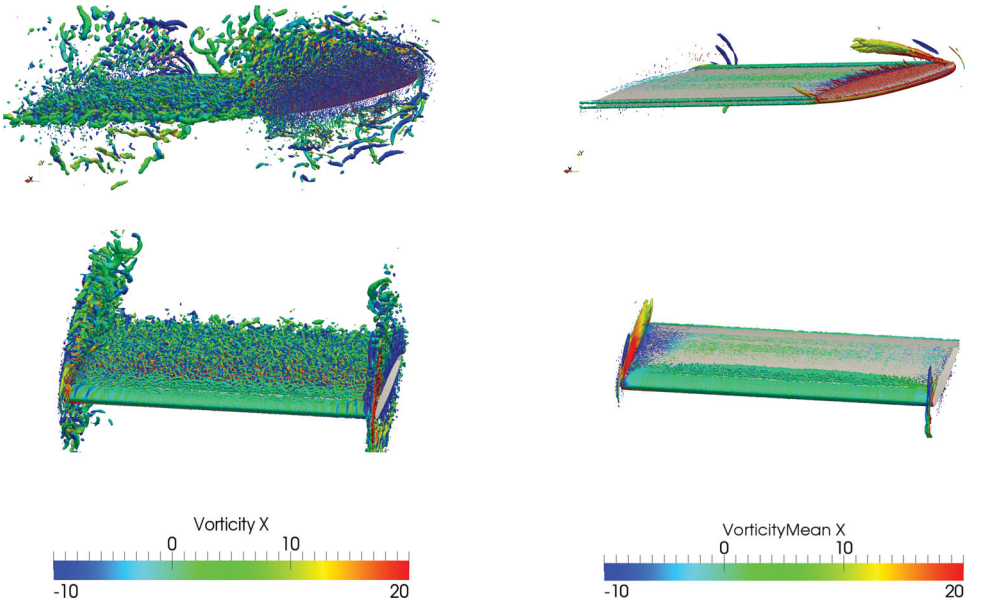

Figure 13. Iso-surface of the non-dimensional Q-criterion (value of 1) using the instantaneous velocity field (left) and the mean velocity field (right). Gap $\tau/c = 0.02$. Downstream view (top) and upstream view (bottom). LES results.

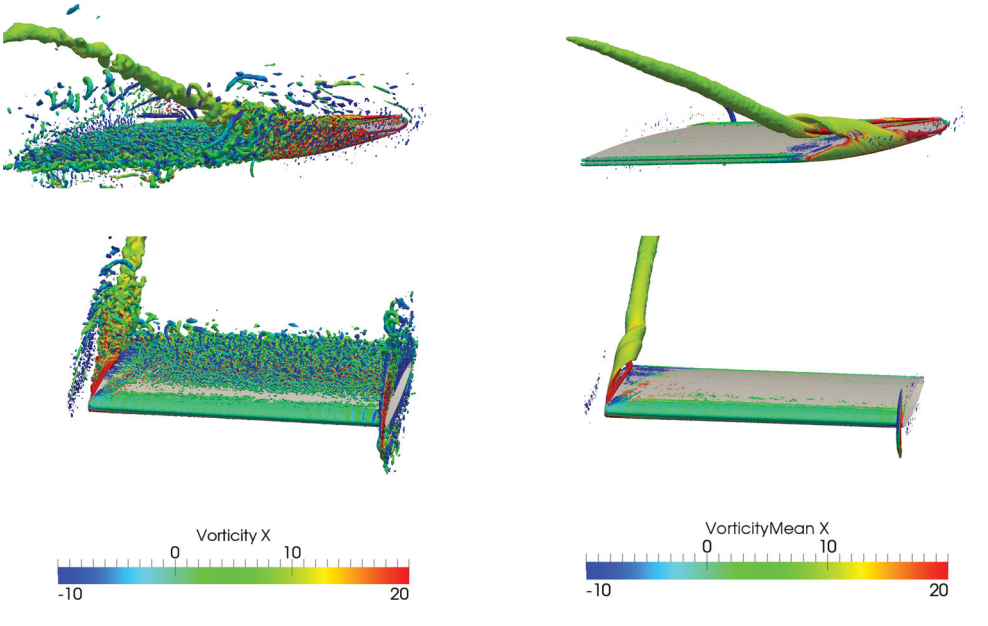

Figure 14. Iso-surface of the non-dimensional Q-criterion (value of 1) using the instantaneous velocity field (left) and the mean velocity field (right). Gap $\tau/c = 0.1$. Downstream view (top) and upstream view (bottom). LES results.

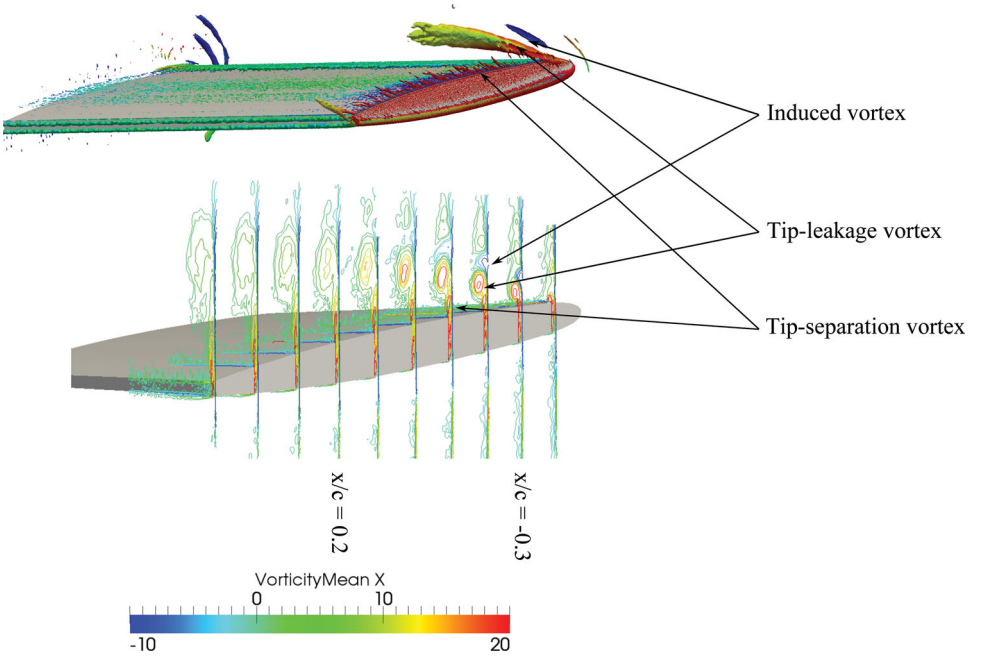

Figure 15. Flow structure for the gap $\tau/c = 0.02$. Iso-surface of the non-dimensional Q-criterion (top, value of 1) and zoom on the iso-lines of the non-dimensional mean axial vorticity ω_x^* (bottom). LES results.

put in evidence: the development of the boundary layer on the blade, the development of the horse shoe vortex on the side opposite to the gap and the vortex structures in the gap region. Regarding the mean flow, the boundary layer is less visible and only the main vortex structures in the gap region are visible. However, for the gap $\tau/c = 0.02$, the vortices that characterised the boundary layer of the endwall still persist contrary to the gap $\tau/c = 0.1$. Furthermore, for the smallest gap, the tip vortex is not visible as a coherent structure in the instantaneous pictures. On the contrary, for the largest gap, the tip vortex is present instantaneously, even if it is not a continuous structure.

The detailed mean vortex structures are shown in Figures 15 and 16 for each gap. Contrary to the previous pictures, the endwall boundary layer is cropped. Strong differences appear between the two gap widths. For the gap $\tau/c = 0.02$, an induced vortex is present contrary to the gap $\tau/c = 0.1$. On the opposite, the tip-separation vortex is well present for the largest gap whereas it is barely developed for the smallest gap. Furthermore, for the gap $\tau/c = 0.1$, the tip-separation vortex wraps the tip-leakage vortex up to the two vortex structures merge into one close to the trailing edge. Regarding the tip-leakage vortex, the strength, the trajectory and the size of the vortex depend on the gap width. As the same value of the Q-criterion and the same iso-lines of the axial vorticity are used for the two gaps, it is noticeable that until the mid-chord of the blade, the vortex strength is higher for the smallest gap. Indeed, the vortex radius that concentrates an axial vorticity larger than $\omega_x^* = 20$ is approximately twice larger for the gap $\tau/c = 0.02$ than the gap $\tau/c = 0.1$. Downstream the mid-chord, the tip-leakage vortex shows a decrease in axial vorticity magnitude from $\omega_x^* \approx 20$ to $\omega_x^* \approx 10$ for the gap $\tau/c = 0.02$, whereas for the second gap this magnitude keeps a value around $\omega_x^* = 20$ up to the trailing edge. The position of the

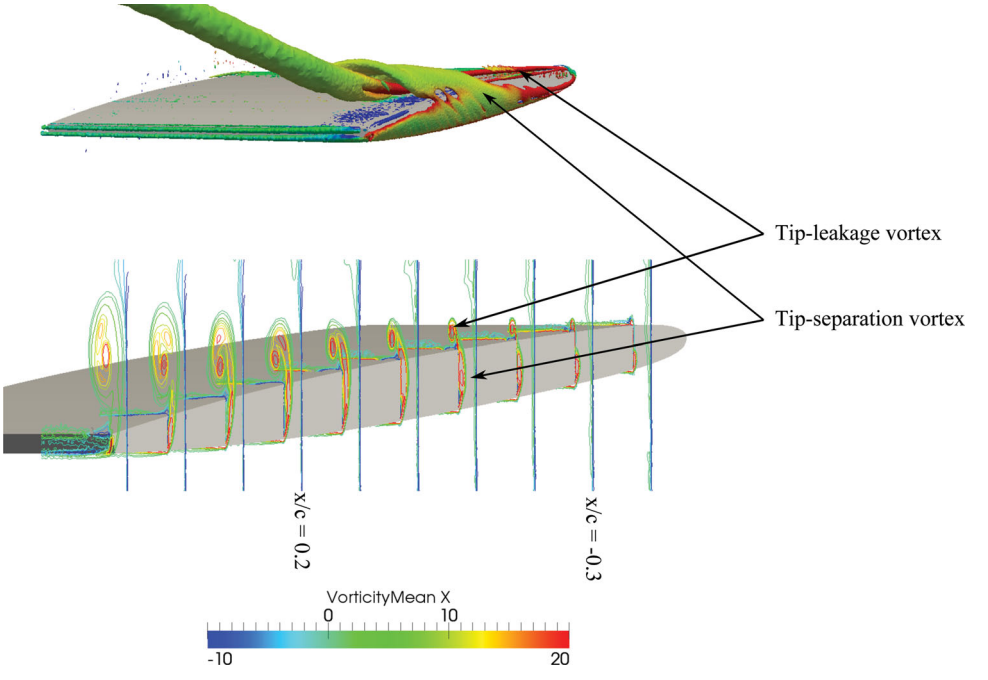

Figure 16. Flow structure for the gap $\tau/c = 0.1$. Iso-surface of the non-dimensional Q-criterion (top, value of 1) and zoom on the iso-lines of the non-dimensional mean axial vorticity ω_x^* (bottom). LES results.

vortex relative to the blade suction side varies with the gap width. For the gap $\tau/c = 0.02$, the vortex moves upward, which is not the case for the gap $\tau/c = 0.1$ since the tip-leakage vortex evolves closely to the suction side as in the unconfined case. Another feature is noticeable for the gap $\tau/c = 0.02$. Looking at the end of the iso-surface, at least, a double structure of the vortex is observed. This feature is also visible on the iso-vorticity lines at the plane $x/c = 0.2$. It seems that the tip-leakage vortex undergoes a kind of deconstruction.

In order to suggest some explanations for these differences between the two gap widths, the contours of the mean velocity components and the mean axial vorticity are represented in Figures 17–20. In addition, inthese figures, the iso-value of the non-dimensional Q-criterion ($Q^* = 1$) is plotted in association with the names of the vortex.

Regarding the gap $\tau/c = 0.02$ (Figures 17 and 20 (left)), several comments can be drawn. First, in the gap region, the axial velocity u_x^* keeps a value close to 1, which indicates that the flow is not decelerated compared to its freestream value. The pitchwise component u_y^* reaches also a value close to 0.8. Therefore, for this configuration, the flow in the gap region looks like a crosswise jet. The flow pattern at the first plane $x/c = -0.3$ allows explaining the formation and the evolution of the tip-leakage vortex and the induced vortex. Due to the pressure difference between the pressure side and the suction side, a leakage jet takes place in the gap. When the jet reaches the suction side of the blade, the flow rolls up due to the pitchwise momentum difference between the jet and the boundary layer that develops on the suction side. As the gap is small, the tip-leakage vortex drags away a part of the boundary layer that develops on the endwall, which leads to the formation of the induced vortex. The axial vorticity of the induced vortex is approximately half the value of the tip-leakage vortex as indicated by the bounds of the colour bar (Figure 20 left). Then, due to

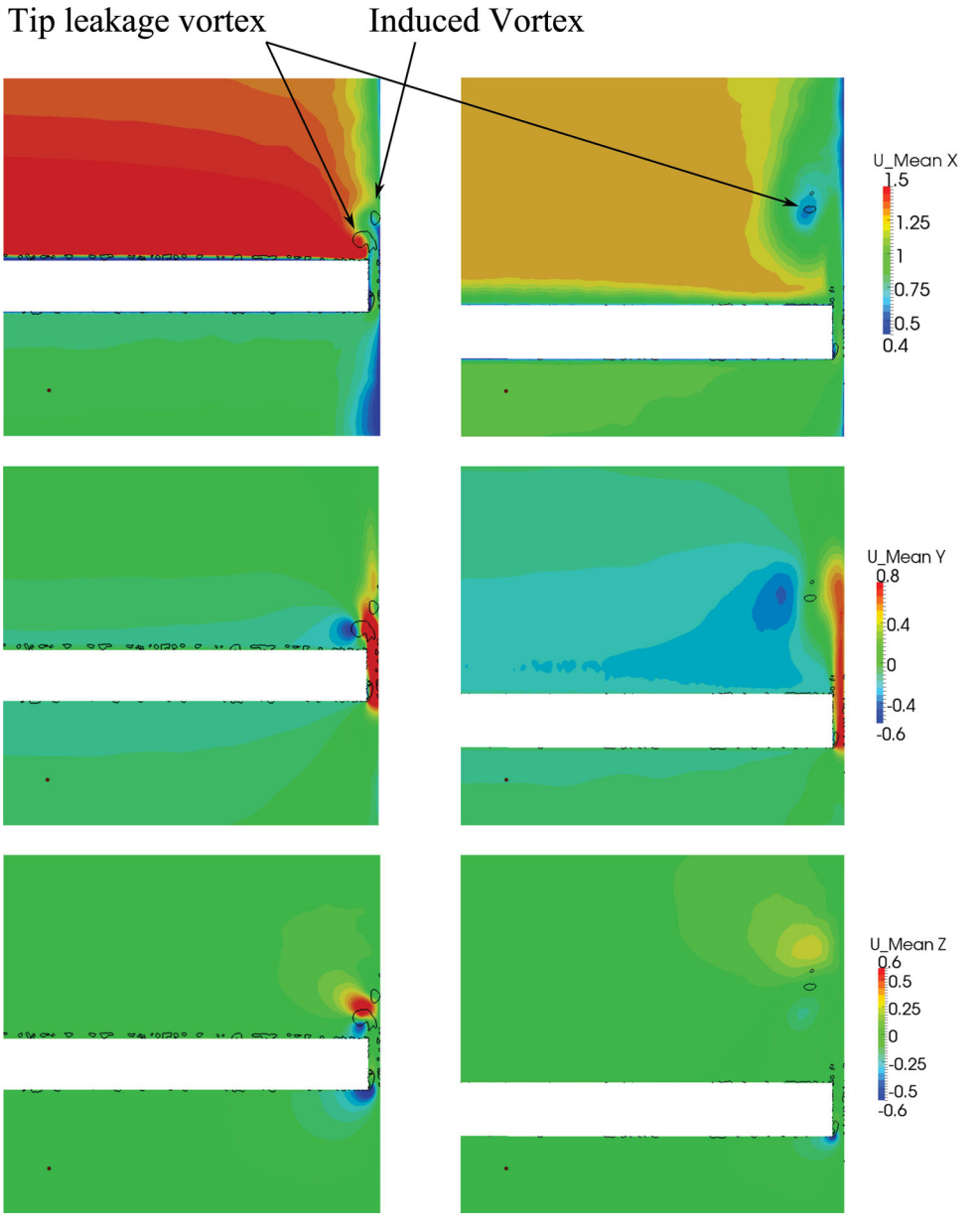

Figure 17. Non-dimensional mean velocity field at $x/c = -0.3$ (left) and $x/c = 0.2$ (right) for the incidence of 10° and the gap $\tau/c = 0.02$. Black lines represent the iso-contour of the non-dimensional Q-criterion ($Q^* = 1$). LES results.

the formation of the tip-leakage vortex, which involves the presence of a spanwise velocity component above the suction side, the leakage jet is confined to a narrow region between the endwall and the tip-leakage vortex. Therefore, the leakage jet leads to the upward displacement of the tip-leakage vortex. For this configuration, no tip-separation vortices are well identified. The vortex structures, which are observed underneath the blade, can be

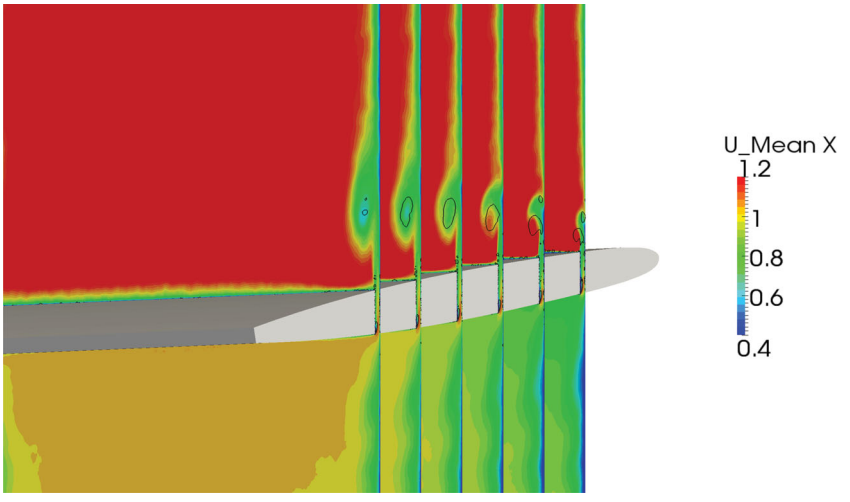

Figure 18. Non-dimensional mean axial velocity field from $x/c = -0.3$ to $x/c = 0.2$ for the incidence of 10° and the gap $\tau/c = 0.02$. Black lines represent the iso-contour of the non-dimensional Q-criterion ($Q^* = 1$). LES results.

interpreted rather as a shear layer than a vortex. Beyond the formation and the evolution of the vortices, another remarkable feature is the decrease in magnitude of the crosswise velocity components between the two planes by a factor of 2. The axial vorticity magnitude also decreases between the two streamwise positions. Moreover, the axial velocity u_x^* reveals an excess of axial momentum at the first plane $x/c = -0.3$, whereas a deficit is present at the second plane $x/c = 0.2$. The excess or deficit in axial momentum is explained by the competition between the vortex circulation and the head losses, at least if a laminar flow is assumed.[43] However, in the present case, the explanation does not come from the vortex core itself. The representation of the axial velocity field along the NACA blade (Figure 18) put in evidence a region of low axial velocity located between the tip-leakage vortex and the induced vortex due to the capture of the wall boundary layer. As the tip-leakage vortex is moving upward, its core ends up capturing this low axial velocity region, which causes the 'deconstruction' of the vortex core.

Focusing on the gap $\tau/c = 0.1$ (Figures 19 and 20 (right)), the flow pattern is quite different from the previous case. First of all, at the plane $x/c = -0.3$, two tip-separation vortices are present underneath the blade. The leakage jet is less intense compared to the smallest gap and the axial flow shows an acceleration in the gap compared to its freestream value. The vortex cores of the tip-leakage and the first tip-separation vortex make in evidence an excess of axial velocity by a factor of 1.5 approximately. No induced vortex is observed, certainly due to the gap width that is too large to allow the capture of the endwall boundary layer by the tip-leakage vortex. At the plane $x/c = 0.2$, the first tip-separation vortex is close to merging with the tip-leakage vortex, whereas the second tip-separation vortex is moving to the suction side. From the first plane to the second plane, the region of a high crosswise velocity magnitude stretches. This is opposite to the observation done at the gap $\tau/c = 0.02$. However, the tip-leakage vortex does not move upward. Several reasons can explain this feature. First, as the gap is larger, the vortex is less influenced by its image in the endwall. Then, the leakage jet is less intense and less confined between the tip-leakage

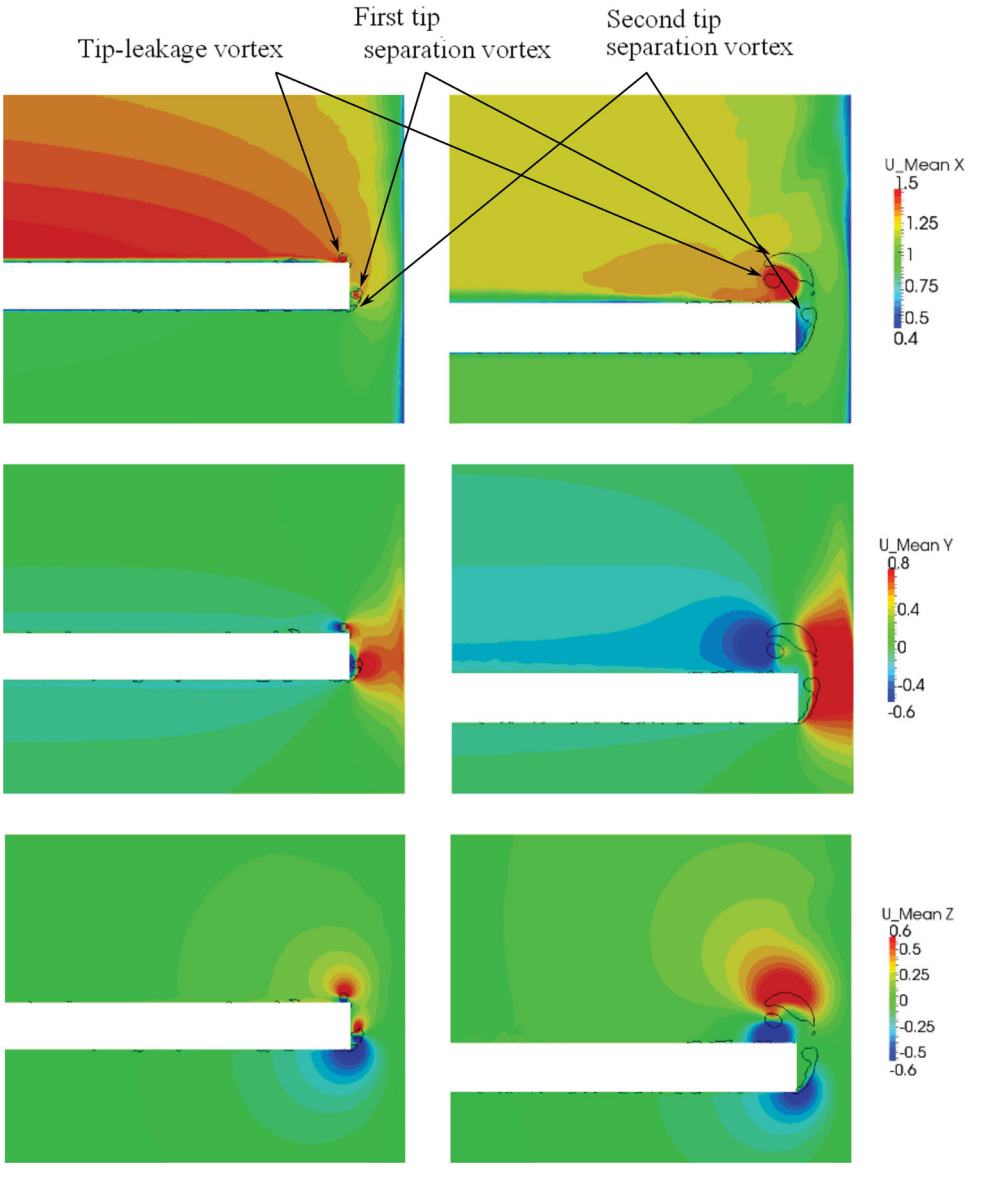

Figure 19. Non-dimensional mean velocity field at $x/c = -0.3$ (left) and $x/c = 0.2$ (right) for the incidence of 10° and the gap $\tau/c = 0.1$. Black lines represent the iso-contour of the non-dimensional Q-criterion ($Q^* = 1$). LES results.

vortex and the endwall, which reduces the jet penetration. Finally, at least from the mid-chord, the tip-leakage vortex is influenced by the tip-separation vortex. As the last one wraps around the tip-leakage vortex, it imposes a downward pitchwise velocity component that prevents the tip-separation vortex to move upward. Opposite to the gap $\tau/c = 0.02$, there is still an excess of streamwise velocity in the tip-leakage vortex core, whereas inside the core of the tip-separation vortex, the value of the non-dimensional streamwise velocity is close to 1.

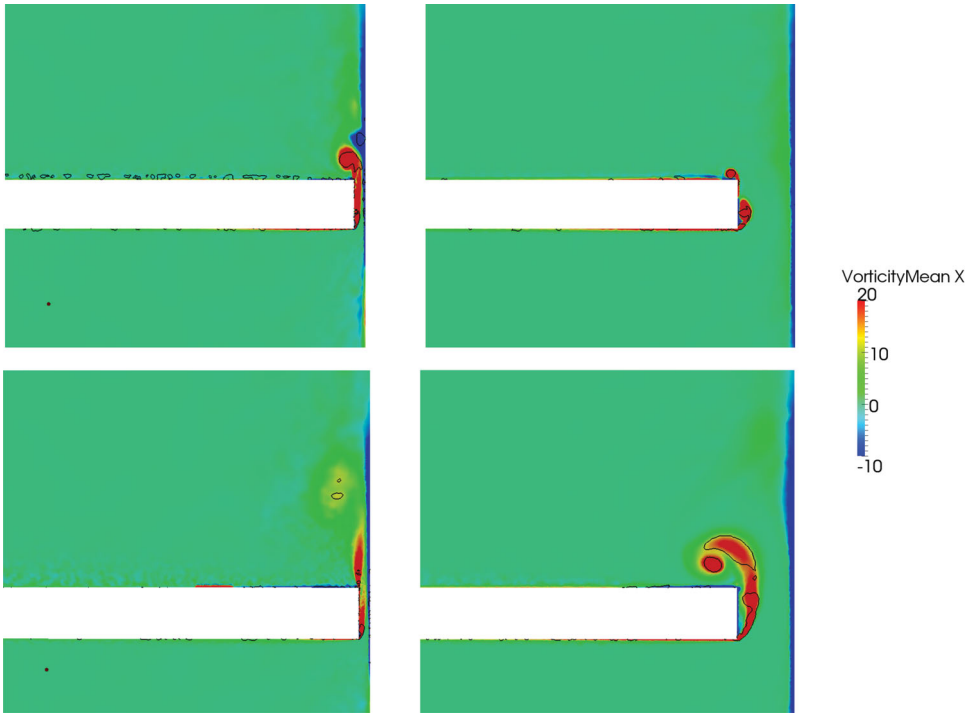

Figure 20. Non-dimensional mean axial vorticity field at $x/c = -0.3$ (top) and $x/c = 0.2$ (bottom) for the incidence of 10° and the gaps $\tau/c = 0.02$ (left) and $\tau/c = 0.1$ (right). Black lines represent the iso-contour of the non-dimensional Q-criterion ($Q^* = 1$). LES results.

The present results are now compared with the study of You et al.,[26] which focuses on a compressor cascade. As the blade shape geometry is different between the two investigations, the results show some agreements and several differences.

In the present study, the flow pattern is depicted with the same three vortices. The mechanisms used to explain the formation of the vortices is rather identical at least for the tip-leakage vortex and the tip-separation vortex. Moreover, an increase in the gap width provokes an increase of the tip-leakage vortex size and an increase in the crosswise velocity and the axial vorticity. These features are true if the flow is considered at the plane $x/c = 0.2$, but it is not true at the first cross plane $x/c = -0.3$.

Despite these agreements, differences appear. First, the presence of the three vortices is not observed simultaneously. The induced vortex is present only for the smallest gap, whereas tip-separation vortices are well developed only for the largest gap. This observation is in contradiction with the computations of You et al., since they observed that the strength of the induced vortex increases with the increase in the gap width. Furthermore, it is mentioned that the tip-leakage vortex and the tip-separation vortex may merge, but the fusion takes place downstream the trailing edge, which it is not the case here. Another difference concerns the fact that increasing the gap width delays the formation of the tip-leakage vortex downstream. In the present work, no delay is captured since the formation of the tip-leakage vortex is located around $x/c \approx -0.45$ for each gap width. Nevertheless (but not shown here), the fusion of the tip-leakage and the tip-separation vortices is delayed with the increase in the gap width. Focusing on the vortex trajectory above the blade, You

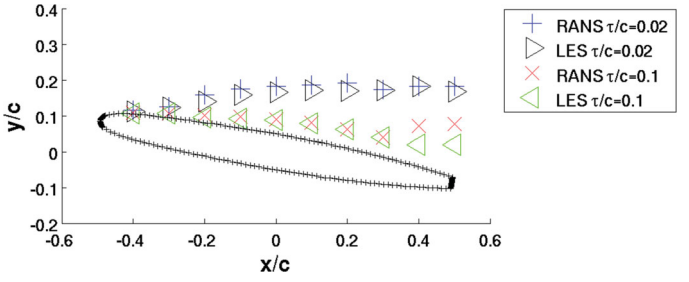

Figure 21. Tip-leakage vortex position in the $x - y$ plane for the NACA0009. RANS and LES results.

et al. observed that the angle between the chord and the vortex core trajectory increases with the increase in the gap width. For the present computations (Figure 21), it is rather the opposite that occurs. However, the angle between the chord and the vortex core trajectory increases with the gap after the fusion of the tip-leakage and tip-separation vortices. It is noticeable that some observations made by You et al. seem to match the present study if the investigation focuses on the flow topology downstream the fusion of the tip-leakage and tip-separation vortices.

To conclude this sub-part, the flow topology is described for two gap widths. A lot of differences are put in evidence between the two configurations, which suggest a strong influence of the gap width on the development and the evolution of the flow. The comparison with the previous study of You et al. [26] shows that a universal picture of the flow topology depending only on the gap width is difficult to bedrawn. Furthermore, the present flow topology is also different from the one proposed by Kang et al.,[14] since no secondary vortex, located between the blade tip and the tip-leakage vortex, is observed. Therefore, additional parameters as maybe the blade geometry should be added to improve the description. Finally, the tip-leakage vortex trajectory plotted in Figure 21 put in evidence that RANS computations are able to capture the position of the vortex in accordance with the LES results. At the trailing edge, for the gap $\tau/c = 0.1$, the differences between the RANS and LES results can be explained by at least two features. First, as the meshes are not the same, a different position of the vortex could be expected. Second, close to the trailing edge, the tip-leakage vortex and the tip-separation vortex merge in one single vortex. The fusion process does not seem to be handled in the same way by the RANS and LES computations.

Nevertheless, the RANS data can be used with confidence to describe at least the trajectory of the vortex for various gap widths, which is the topic of the following sub-part.

4.3. *The tip-leakage vortex trajectory*

In 1991, Chen [44] proposed a linear law for the pitchwise trajectory of the tip-leakage vortex above a plate. Other authors proposed a formulation for the tip-leakage vortex trajectory in a turbomachinery involving further parameters.[45] However, the increase in complexity does not improve the model as suggested by the experimental work of Roussopoulos.[3]

In the model of Chen, the trajectory of the tip-leakage vortex is defined in the system of reference displayed in Figure 22. The streamwise position x_1 is determined from the leading edge and the pitchwise position y_1 is measured from the chord. The law is derived semi-empirically. First, a non-dimensional analysis of the flow based on the time-dependant

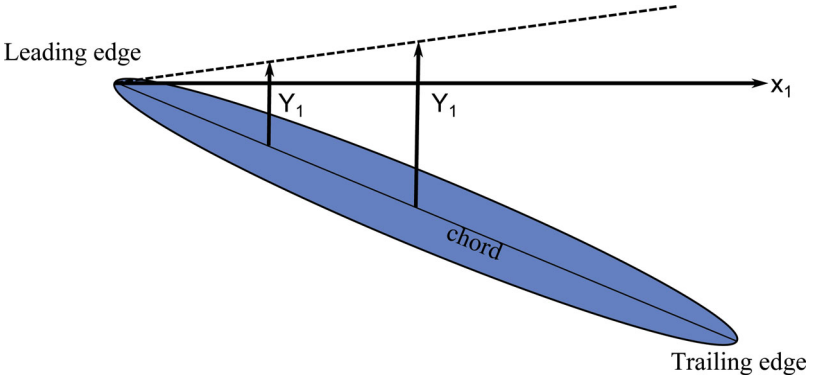

Figure 22. System of reference $x_1 - y_1$ used for the tip-leakage vortex trajectory.

two-dimensional Euler equations shows that only one non-dimensional parameter t^* can be formed:

$$t^* = \frac{t}{\tau}\sqrt{\frac{\overline{\Delta p}}{\rho}} \tag{8}$$

with

- $\overline{\Delta p}$ the mean pressure difference between the pressure side and the suction side.
- $t = x_1/u_x$ the time with u_x the streamwise velocity.
- τ the gap width.

Then, gathering various data, it was found that the non-dimensional pitchwise position $y_1^* = y_1/\tau$ can be related linearly to the non-dimensional time t^*:

$$y_1^* = K\, t^* \tag{9}$$

with $K = 0.46$. However, using this relation, Kang et al. [15] suggest for their experiment the value of $K = 0.19$.

The Chen model can be also expressed in a non-dimensional spatial system of reference $x_1^* - y_1^*$. Defining the non-dimensional distance $x_1^* = x_1/c$ and the mean pressure coefficient $Cp_m = \frac{\overline{\Delta p}}{1/2\rho u_x^2}$, the non-dimensional time t^* reads

$$t^* = \sqrt{\frac{Cp_m}{2}}\,\frac{c}{\tau}\,x_1^* \tag{10}$$

and the tip-leakage vortex trajectory becomes

$$y_1^* = K\sqrt{\frac{Cp_m}{2}}\,\frac{c}{\tau}\,x_1^* \tag{11}$$

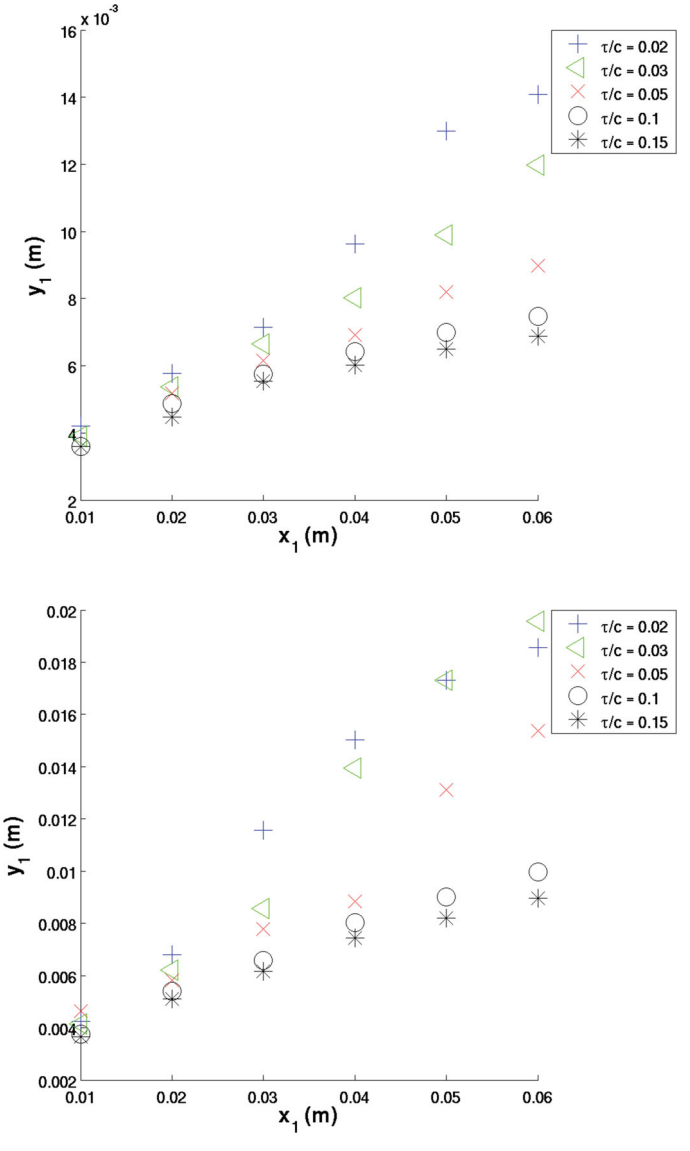

Figure 23. Pitchwise position of the vortex centre above the blade (NACA0009) in the $x_1 - y_1$ plane. Incidences of 5° (top) and 10° (bottom). RANS results.

In the dimensional system of reference $x_1 - y_1$, the position y_1 of the tip-leakage vortex centre is

$$y_1 = K \sqrt{\frac{Cp_m}{2}}\, x_1 \tag{12}$$

This relation shows that the pitchwise position of the tip-leakage vortex is independent of the gap width.

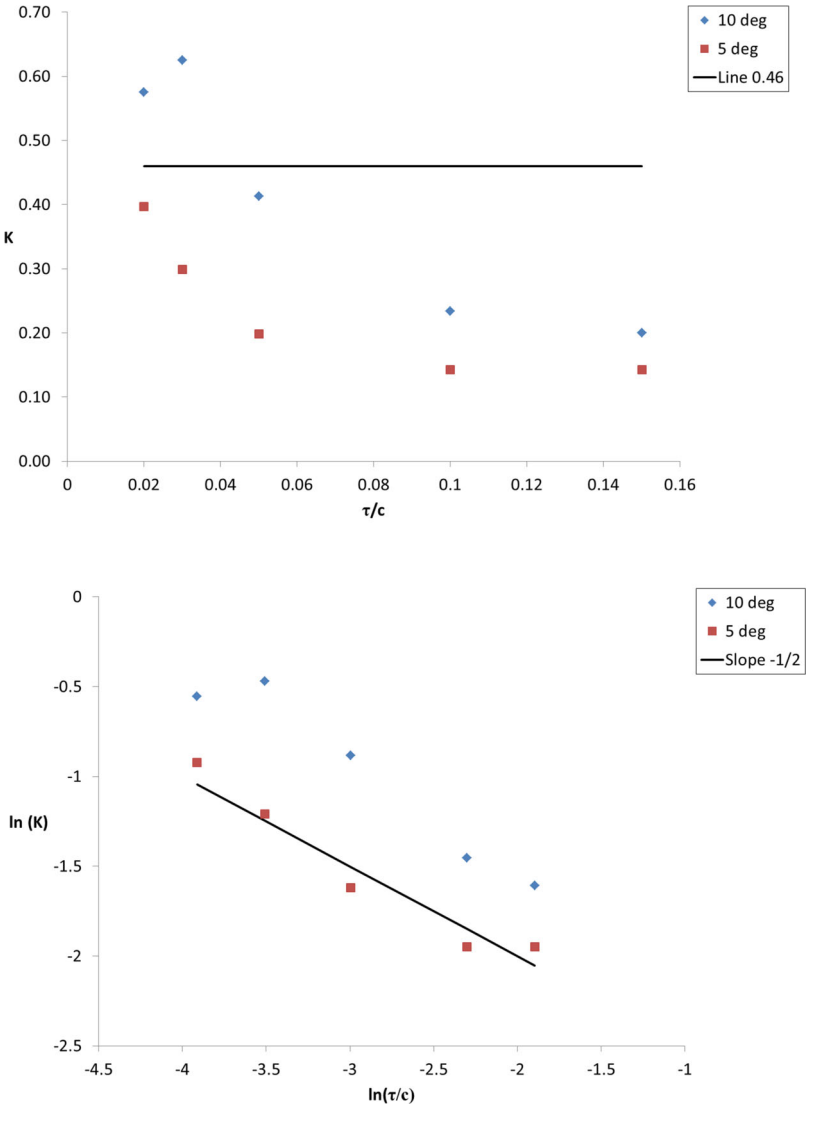

Figure 24. Coefficient K from the model of Chen for each flow configuration (NACA0009). Linear scale (top) and logarithmic scale (bottom).

For the present study, the tip-leakage vortex trajectory in the system of reference $x_1 - y_1$ is plotted in Figure 23. The plot is stopped before the fusion of the tip-leakage and tip-separation vortices (at $x_1 \approx 0.06$ m). It is noticeable that the trajectory of the tip-leakage vortex depends on the gap width. Therefore, the model of Chen cannot be used. Nevertheless, the tip-leakage vortex seems to follow a linear trajectory. Applying a linear interpolation of the numerical data, the slope s is determined for each flow configuration. Then, the Chen coefficient K is computed for each flow configuration as

$$K = \frac{s}{\sqrt{\frac{Cp_m}{2}}} \tag{13}$$

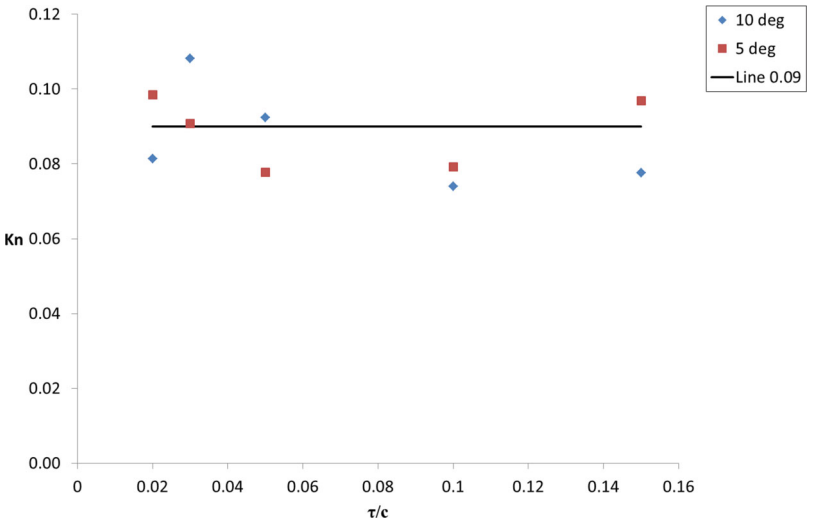

Figure 25. New coefficient K_n for each flow configuration (NACA0009).

The values are represented in Figure 24 using a linear and a logarithmic scale. The linear plot put in evidence that the coefficient K is not constant and deviates significantly from the value of 0.46 proposed by Chen. The logarithmic plot shows that the points are aligned along a line with a slope of approximately $-1/2$. Therefore, the coefficient K decreases approximately as $1/\tau^{1/2}$.

Starting from this observation, a new model is empirically derived, introducing dependence between gap width and tip-leakage vortex position. Setting $y_1^* = y_1/\tau$ and $x_1^* = x_1/c$, the following relation is proposed:

$$y_1^* = K_n \sqrt{\frac{Cp_m}{2}} \left(\frac{c}{\tau}\right)^{3/2} x_1^* \tag{14}$$

A factor of $\sqrt{c/\tau}$ differentiates the above equation and the model of Chen (Equation (11)). Figure 25 represents the values of the coefficient K_n for each flow configuration. From these data, a mean value of $K_n \approx 0.09$ is estimated.

Defining

$$l^* = \sqrt{\frac{Cp_m}{2}} \left(\frac{c}{\tau}\right)^{3/2} x_1^* \tag{15}$$

the tip-leakage vortex trajectory can be expressed as a linear relation between y_1^* and l^*

$$y_1^* = 0.09\, l^* \tag{16}$$

Figures 26 and 27 display the tip-leakage vortex trajectory for each flow configuration using the representation of Chen (Equation (11)) and the new representation (Equation (16)). Data obtained from the simulation of a NACA0015 at an incidence of 10° and for two gaps (2 and 10 mm) are added in Figure 26. To allow a better comparison between the two models, the values of t^* and l^* are re-centred between 0 and 1, which modifies

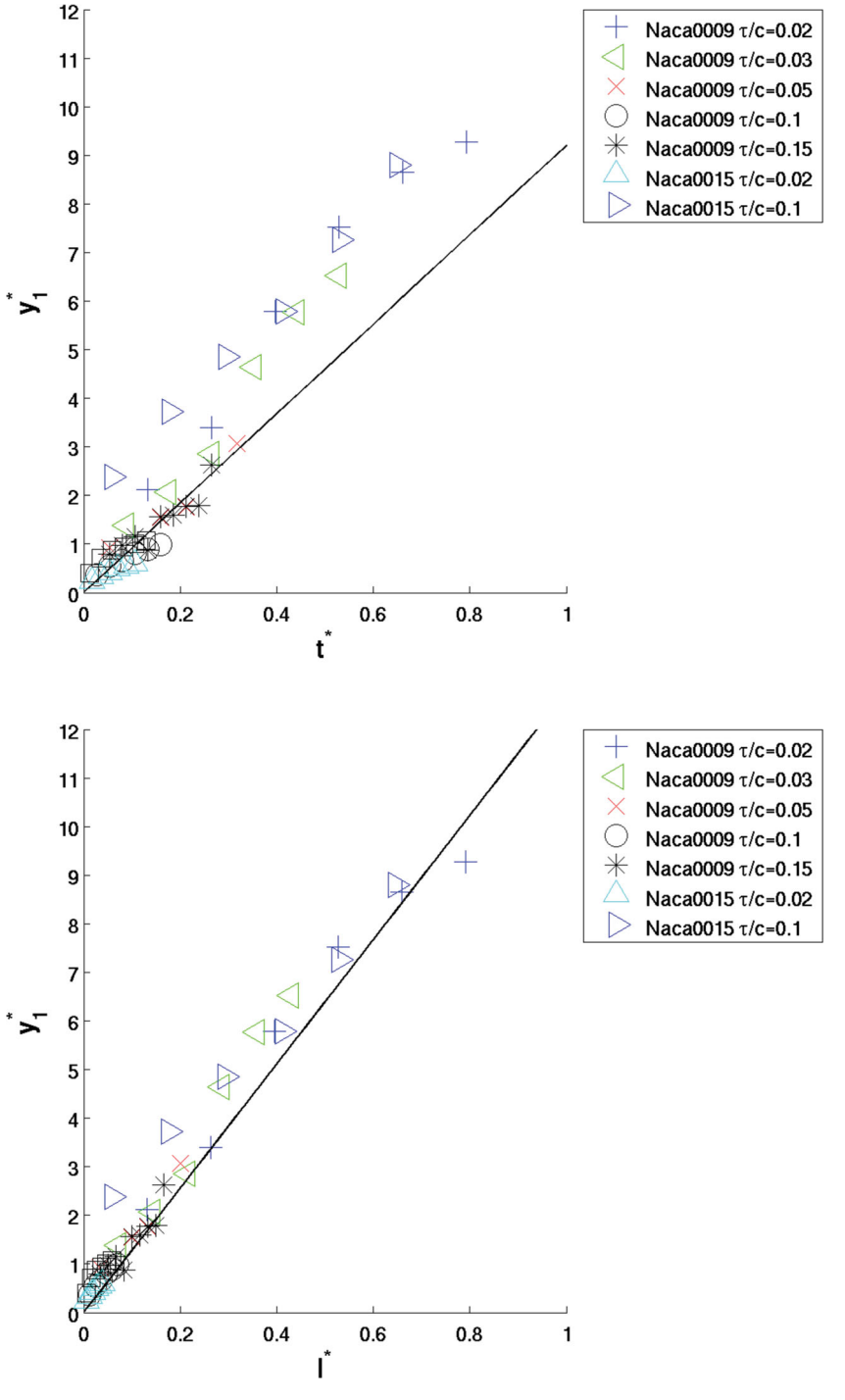

Figure 26. Vortex trajectory for the NACA0009 and NACA0015 at an incidence of 10° using the representation of Chen (top) and the new representation (bottom). RANS results. The black line refers to the model.

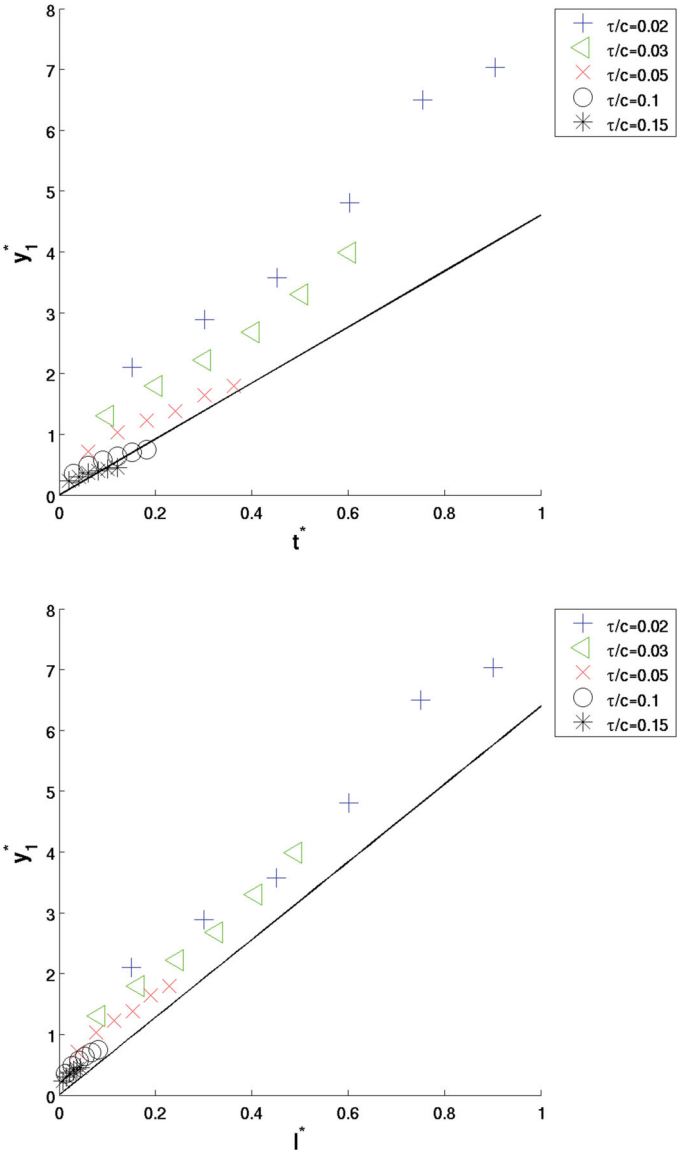

Figure 27. Vortex trajectory for the NACA0009 at an incidence of 5° using the representation of Chen (top) and the new representation (bottom). RANS results. The black line refers to the model.

the original slope of the models. The correspondences between the initial slope and the modified slope are referenced in Table 2. The new formulation provides a better collapse of all the data even if a correction at the origin will be needed. Using the Chen formulation, the data do not collapse and the slope changes depending on the gap width particularly for the incidence of 5°. As the data from the NACA0015 collapse with the NACA0009 data, the new formulation can be considered as independent of the blade geometry. Furthermore, a computation (not represented in the figure to avoid an overwriting) of the NACA0009

Table 2. Correspondence between the original slopes of the models and the slopes for the re-centred plots between 0 and 1.

	Original slope	Slope for the incidence of 5°	Slope for the incidence of 10°
Chen's model	0.46	4.6	9.2
New model	0.09	6.4	12.8

blade with a chord twice longer than in the present case does not show an influence of the chord length.

5. Conclusion

Several LES and RANS computations of a NACA0009 blade including the gap between the tip and the endwall have been performed and analysed. The LES computations are mainly devoted to investigate the flow topology in the gap region. Due to the computational cost of such simulations, only one incidence (10°) and two gaps ($\tau/c = 0.02$ and $\tau/c = 0.1$) have been simulated. The RANS computations are used to investigate the trajectory of the tip-leakage vortex. Five gap widths (from $\tau/c = 0.02$ to $\tau/c = 0.15$) and two incidences (5° and 10°) have been computed.

First, the RANS and LES computations are compared with the experimental data available downstream the blade. The results show a qualitative and quantitative agreement. The vortex core trajectory is captured with confidence. Furthermore, at least outside the vortex core, the velocity and vorticity fields are in agreement with the experimental measurements as shown for instance by the collapse of the iso-lines of the axial vorticity.

The LES computations are analysed to describe the flow topology in the gap zone. It is put in evidence that the gap width influences the development of the vortex flow. For the smallest gap ($\tau/c = 0.02$), an induced vortex is captured, whereas no tip-separation vortices are observed. The tip-leakage vortex moves upward the suction side and shows a kind of deconstruction of its core. This deconstruction is explained by the interaction between the tip-leakage vortex core and the low axial momentum region originating from the capture of the endwall boundary layer. For the largest gap ($\tau/c = 0.1$), no induced vortex is observed, whereas a fusion between the tip-leakage vortex and the tip-separation vortex is depicted. Contrary to the smallest gap, the vortex core does not show a decrease in the streamwise velocity. Therefore, the vortex core is sustained all along the vortex life. Compared to the results provided by You et al,[26,27] some agreements are observed and several differences are underlined. Among the agreements, the two studies put in evidence the same vortices and the same mechanisms to explain the formation of the vortex flow in the gap region. Among the differences, it can be mentioned that the formation of the tip-leakage jet is not delayed with an increase in the gap width. You et al. investigate a compressor cascade with a blade curvature higher than in the present study, which could explain the differences.

The last part of the results deals with the trajectory of the tip-leakage vortex. Starting from the work of Chen [44] and using the RANS results for several flow configurations, a semi-empirical law is deduced. This law is able to fit the trajectory of the core of the tip-leakage vortex whatever is the gap width, the blade incidence and the blade geometry since a NACA0015 has been also computed. In case of cavitation, such a law could be useful to determine if the vortex will interact with the endwall and cause damages due to erosion.

For future works, the investigation of the blade curvature will be suitable both to clarify the flow topology between the present computations and those carried out by You et al. and to enlarge or to restrict the range of application of the law proposed to describe the trajectory of the tip-leakage vortex.

Acknowledgements

Vincent Moureau and Ghislain Lartigue from the CORIA lab, and the SUCCESS scientific group are acknowledged for providing the YALES2 code.

Disclosure statement

No potential conflict of interest was reported by the authors.

Funding

The authors are very grateful to the Competence Center in Energy and Mobility (CCEM), Swisselectric Research and the foundation The Ark through the programme The Ark Energy for their financial support. A part of this work was performed using HPC resources from GENCI-IDRIS [grant number 2012-020611].

References

[1] Muthanna C, Devenport WJ. Wake of a compressor cascade with tip gap, part 1: mean flow and turbulence structure. AIAA J.2004;42:2320–2331.
[2] Miorini RL, Katz J. The internal structure of the tip leakage vortex within the rotor of an axial waterjet pump. J Turbomach. 2012;134.
[3] Roussopoulos K, Monkewitz PA. Measurements of tip vortex characteristics and the effect of an anti-cavitation lip on a model Kaplan turbine blade. Flow Turbul Combust.2000;64:119–144.
[4] Rains DA. Tip clearance flows in axial compressors and pumps. Pasadena, CA: California Institute of Techonology; 1954.
[5] Lakshminarayana B, Ravindranath A. Interaction of compressor rotor blade wake with wall boundary layer/vortex in the end-wall region. J Eng Gas Turbines Power.1982;104:467–478.
[6] Lakshminarayana B, Pouagare M, Davino R. Three-dimensional flow-field in the tip region of a compressor rotor passage, part 1: mean velocity profiles and annulus wall boundary layer. J Eng Gas Turbines Power.1982;104:760–771.
[7] Lakshminarayana B, Pouagare M, Davino R. Three-dimensional flow-field in the tip region of a compressor rotor passage, part 2: turbulence properties. J Eng Gas Turbines Power.1982;104:772–781.
[8] Lakshminarayana B, Pandya A. Tip clearance flow in a compressor-rotor passage at design and off-design conditions. J Eng Gas Turbines Power.1984;106:570–577.
[9] Pandya A, Lakshminarayana B. Investigation of the tip clearance flow inside and at the exit of a compressor rotor passage. Part 1: mean velocity field. J Eng Gas Turbines Power.1993;105:1–12.
[10] Pandya A, Lakshminarayana B. Investigation of the tip clearance flow inside and at the exit of a compressor rotor passage. Part 2: turbulence properties. J Eng Gas Turbines Power.1993;105:13–17.
[11] Davino R. Characteristics of the flow in the annulus wall region of an axial-flow compressor rotor blade passage. Orlando, FL; 1982. (AIAA Paper 82-0413).
[12] Inoue M, Kuroumaru M. Structure of tip clearance flow in an isolated axial compressor rotor. J Turbomach. 1989;111:250–256.
[13] Goto A. Three-dimensional flow and mixing in axial flow compressor with different rotor tip clearances. J Turbomach.1992;114:675–685.

[14] Kang S, Hirsch C. Experimental study on the three-dimensional flow within a compressor cascade with tip clearance: part I – velocity and pressure fields. J Turbomach.1993;115: 435–467.
[15] Kang S, Hirsch C. Experimental study on the three-dimensional flow within a compressor cascade with tip clearance: part II – the tip leakage vortex. J Turbomach.1993;115: 444–452.
[16] Puddu P. Tip leakage flow characteristics downstream of an axial flow fan. American Society of Mechanical Engineers; 1996. (Paper 96-Gt-508).
[17] Kang S, Hirsch C. Tip leakage flow in linear compressor cascade. J Turbomach.1994;116: 657–664.
[18] Wang Y, Devenport WJ. Wake of a compressor cascade with tip gap, part 2: effects of endwall motion. AIAA J.2004;42:2332–2340.
[19] Kang S, Hirsch C. Numerical simulation of three-dimensional viscous flow in a linear compressor cascade with tip clearance. J Turbomach.1996;118:492–505.
[20] Shin S. Reynolds-averaged Navier-Stokes computation in a tip clearance flow in a compressor cascade using an unstructured grid. Blacksburg (VA): Faculty of the Virginia Polytechnic Institute and State University; 2001.
[21] Kato H, Taniguchi H, Matsuda K, Funazaki KI, Kato D, Pallot G. Experimental and numerical investigation on compressor cascade flows with tip clearance at a low Reynolds number condition. J Thermal Sci.2011;20:481–485.
[22] Corsini A, Rispoli F. Flow analyses in a high-pressure axial ventilation fan with a non-linear eddy-viscosity closure. Int J Heat Fluid Flow.2005;26:349–361.
[23] Borello D, Hanjalic K, Rispoli F. Computation of tip-leakage flow in a linear compressor cascade with a second-moment turbulence closure. Int J Heat Fluid Flow.2007;28:587–601.
[24] You D, Mittal R, Wang M. Progress in large-eddy simulation of a rotor tip-clearance flow. 12th Annual DoD HPCMP User Group Conference. Austin, TX; 2002.
[25] You D. Computational methodology for large-eddy simulation of tip-clearance flows. AIAA J. 2004;271–279.
[26] You D, Wang M, Moin P, Mittal R. Effects of tip-gap size on the tip-leakage flow in a turbomachinery cascade. Phys Fluids. 2006;18.
[27] You D, Wang M, Moin P, Mittal R. Large-eddy simulation analysis of mechanisms for viscous losses in a turbomachinery tip-clearance flow. J Fluid Mech.2007;586:177–204.
[28] Dreyer M, Decaix J, Münch C, Farhat M. Mind the gap – a new insight on the tip leakage vortex using stereo PIV. Exp Fluids. 2014;55. doi:10.1007/s00348-014-1849-7
[29] Menter F. Two-equation eddy-viscosity turbulence models for engineering applications. AIAA J.1994;32:1598–1605.
[30] Weller H, Tabor G, Jasak H, Fureby C. A tensorial approach to computational continuum mechanics using objected-oriented techniques. Comput Phys.1998;12:620–631.
[31] Patankar S. Numerical heat transfer and fluid flow. Washington DC: Hemisphere; 1981.
[32] Rhie C, Chow W. Numerical study of the turbulent flow past an airfoil with trailing edge separation. AIAA J. 1983;1525–1532.
[33] Harten A. High resolution schemes for hyperbolic conservation laws. J Comput Appl Math.1983;49:357–393.
[34] Germano M, Piomelli U, Moin P, Cabot W. A dynamic subgrid-scale eddy viscosity model. Phys Fluids A. 1991;3.
[35] Moureau V, Domingo P, Vervisch L. From large-eddy simulation to direct numerical simulation of a lean premixed swirl flame: filtered laminar flame-PDF modeling. Combust Flame.2011;158:1340–1357.
[36] Moureau V, Domingo P, Vervisch L. Design of a massively parallel CFD code for complex geometries. Comptes Rendus Mécanique. 2011;339:141–148.
[37] Duprat C, Balarac G, Métais O, Congedo PM, Brugière O. A wall layer model for large-eddy simulations of turbulent with/out pressure gradient. Phys Fluids. 2011;23.
[38] Maheu N, Moureau V, Domingo P, Duchaine F, Balarac G. Large-eddy simulations of flow and heat transfer around a low-Mach number turbine blade. Proceeding of the Stanford CTR Summer Program. Standford University; 2012.
[39] Wang M, Moin P. Dynamic wall modeling for large-eddy simulation of complex turbulent flows. Phys Fluids.2002;14:2043–2051.
[40] Abbot I, von Doenhoff A, Albert E. Summary of airfoil data. 1945. (NACA Report 824).

[41] Avellan F, Henry P, Ryhming I.L. A new high speed cavitation tunnel. International Symposium on Cavitation Research Facilities and Techniques, ASME Winter Annual Meeting. Proceedings; Boston, MA; 1987. p. 49–60.
[42] Lakshminarayana B. Fluid dynamics and heat transfer of turbomachinery. New York (NY): Wiley Interscience; 1996.
[43] Batchelor G. Axial flow in trailing line vortices. J Fluid Mech.1964;20:645–658.
[44] Chen GT. Vortical structures in turbomachinery tip clearance flows. Cambridge (MA): Massachusetts Institute of Technology; 1991.
[45] Song SJ, Martinez-Sanchez M. Rotordynamic forces due to turbine tip leakage, part I: blade scale effects. J Turbomach.1997;119:695–703.